DEPARTMENT OF TRANSPORTATION

Displacement Monitoring of I-35W Saint Anthony Falls Bridge with Current Vibration-Based System

Lauren Linderman, Principal Investigator
Department of Civil, Environmental, and Geo- Engineering
University of Minnesota

January 2019

Research Project
Final Report 2019-05

To request this document in an alternative format, such as braille or large print, call 651-366-4718 or 1-800-657-3774 (Greater Minnesota) or email your request to ADArequest.dot@state.mn.us. Please request at least one week in advance.

Technical Report Documentation Page

1. Report No.	2.	3. Recipients Accession No.	
MN/RC 2019-05			
4. Title and Subtitle Displacement Monitoring of I-35W Saint Anthony Falls Bridge with Current Vibration-Based System		5. Report Date January 2019 6.	
7. Author(s) Riley J. Brown, Karl O. Gaebler, Carol K. Shield, Lauren E. Linderman		8. Performing Organization Report No.	
9. Performing Organization Name and Address Department of Civil, Environmental, and Geo- Engineering University of Minnesota 500 Pillsbury Drive SE Minneapolis, MN 55455		10. Project/Task/Work Unit No. CTS#2017006 11. Contract (C) or Grant (G) No. (c) 99008 (wo) 237	
12. Sponsoring Organization Name and Address Minnesota Department of Transportation Research Services & Library 395 John Ireland Boulevard, MS 330 St. Paul, Minnesota 55155-1899		13. Type of Report and Period Covered Final Report 14. Sponsoring Agency Code	
15. Supplementary Notes http://mndot.gov/research/reports/2019/201905.pdf			

16. Abstract (Limit: 250 words)

Since the opening of the I-35W Saint Anthony Falls Bridge in 2008, over 500 sensors have been collecting data to better understand the behavior of post-tensioned concrete box girder structures. Recent research in the accelerometers installed on the bridge indicates they can be effectively used in a vibration-based structural health monitoring system, but previous studies have shown that natural frequency alone may not be sufficient to determine the performance of the structure. Vertical displacements were believed to be a simpler performance measure as direct comparisons can be made with design calculations and maintenance guidelines. To avoid the shortcomings of conventional displacement measurement options, this study focuses on using the currently installed accelerometers to estimate the vertical displacements of the southbound bridge. The proposed technique utilizes up-to-date modal parameters within a dual Kalman filter to estimate the vertical displacements of the structure from noisy acceleration measurements. When applied to the I-35W Saint Anthony Falls Bridge, it was found that the dual Kalman filter approach captures only dynamic displacements due to relatively slow loading (e.g., traffic loading and thermal loading) and the corresponding low-frequency static displacements are likely too small for GPS measurements due to the high stiffness of the structure.

17. Document Analysis/Descriptors	18. Availability Statement		
Structural health monitoring, Estimation Theory, Kalman Filtering	No restrictions. Document available from: National Technical Information Services, Alexandria, Virginia 22312		
19. Security Class (this report) Unclassified	20. Security Class (this page) Unclassified	21. No. of Pages 72	22. Price

DISPLACEMENT MONITORING OF I-35W SAINT ANTHONY FALLS BRIDGE WITH CURRENT VIBRATION-BASED SYSTEM

FINAL REPORT

Prepared by:

Riley J. Brown
Karl O. Gaebler
Carol K. Shield
Lauren E. Linderman
Department of Civil, Environmental, and Geo- Engineering
University of Minnesota

January 2019

Published by:

Minnesota Department of Transportation
Research Services & Library
395 John Ireland Boulevard, MS 330
St. Paul, Minnesota 55155-1899

TABLE OF CONTENTS

CHAPTER 1: Introduction 1

CHAPTER 2: Bridge Description and Instrumentation 2

CHAPTER 3: Previous Monitoring Works 4

CHAPTER 4: Displacement Estimation Using the Kalman Filter 7

4.1 System model equations and the dual Kalman filter 8

4.1.1 State-Space System Equations 8

4.1.2 Output-Only Implementation 10

4.1.3 Discrete-Time Stochastic State-Space Equations 10

4.1.4 Dual Kalman Filter for Input and State Estimation 11

4.2 Tuning the dual Kalman filter 11

4.2.1 Simulated System 12

4.2.2 Tuning Qx and Qp 12

4.2.3 Tuning When No Noise is Present 13

4.2.4 Tuning When Model Noise and Measurement Noise is Present 14

4.2.5 Tuning Conclusions 17

4.3 Blind case study 17

4.4 Advantages of the dual Kalman filter when inputs are not of interest 18

4.4.1 Simulated Example 19

4.4.2 Experimental Test 19

4.5 A summary of displacement estimation using a dual Kalman filter 20

CHAPTER 5: I-35W Bridge Displacement Estimation 34

5.1 Tuning the DKF for I-35W Bridge Displacement Estimation 34

5.2 Event Detection 35

5.3 Event Detection on I-35W Bridge Displacement Estimates 36

CHAPTER 6: Estimating Moving Loads 40

CHAPTER 7: Summary and Conclusions 44

REFERENCES 46

APPENDIX A Monitoring System Outages

APPENDIX B The Dual Kalman Filter

LIST OF FIGURES

Figure 2.1: Elevation view of the I-35W Saint Anthony Falls Bridge (French et al. 2012) 3

Figure 2.2: Long-term accelerometer layout used from May 11, 2010 until present (French et al. 2012) .. 3

Figure 3.1: Southbound structure F.E.A. estimated mode shapes 1 through 4 (French et al. 2012) 5

Figure 3.2: Monthly average natural frequency of modes 1 through 4 (Gaebler, Shield, and Linderman 2017) 5

Figure 3.3: Southbound structure identified mode shapes 1 through 4 (Gaebler, Shield, and Linderman 2017) 6

Figure 4.1: Simulated 8 degree of freedom system 21

Figure 4.2: Displacement estimate range at node 4 21

Figure 4.3: Power spectrum of displacement estimates 22

Figure 4.4: (a) Acceleration estimation error surface. Clean model, measurements. 2% damping. (b) Displacement estimation error surface. Clean model, measurements. 2% damping 23

Figure 4.5: Top-down view of acceleration error surface. Flat regions (red) identify a region of tuning parameters that generate all possible displacement estimates (black) 24

Figure 4.6: Mode shapes for clean and noisy model 24

Figure 4.7: Displacement estimate using truncated model at node 4 25

Figure 4.8: Displacement estimation error tuning surface. Clean model, noisy measurements (SNR = 20). 2% damping 25

Figure 4.9: Displacement estimate at node 4 from noisy measurements (SNR = 20) 26

Figure 4.10: Blind case study system 26

Figure 4.11: Acceleration estimation error surface for blind case study system 26

Figure 4.12: Displacement estimate range at node 3 for blind case study system 27

Figure 4.13: Input estimates at node 3 for blind case study system 27

Figure 4.14: Comparison of displacement estimate from dual Kalman filter (DKF) for blind case study system at node 3 28

Figure 4.15: Displacement estimates from dual Kalman filter (DKF) and single Kalman filter (KF) at node 4, random excitation 28

Figure 4.16: (a) Acceleration estimation error for single Kalman filter. Clean model, measurements. 2% damping, random excitation. (b) Displacement estimation error for single Kalman filter. Clean model, measurements. 2% damping, random excitation 29

Figure 4.17: Displacement estimates from dual Kalman filter (DKF) and single Kalman filter (KF) at node 4 – impulse excitation 30

Figure 4.18: Laboratory experimental set up 30

Figure 4.19: Schematic drawing of experimental setup and sensor locations 31

Figure 4.20: Beam-column connection with accelerometer and LVDT attachment 31

Figure 4.21: Displacement estimates from dual Kalman filter (DKF) and single Kalman filter (KF) at node 4 for experimental system 32

Figure 5.1: Acceleration estimation error surface for I-35W Bridge 37

Figure 5.2: Displacement estimate range at SB SP 2 Ext for I-35W Bridge 'Open S7' dynamic truck test . 37

Figure 5.3: 'Open S9' event detection (Top) Displacement estimate with event detection (light blue) and corresponding RMS (Bottom) RMS of displacement estimate, used to identify events 38

Figure 5.4: Event detection set limits (Left) Event detection with too high RMS peak magnitude limit (Right) Event detection with too low of a cutoff limit 38

Figure 5.5: Detrending drifted displacement estimate for event detection (Left) Event detection on drifted displacement estimates (Right) Event detection on detrended displacement estimate record.... 39

Figure 6.1: Br. 27568 simulated maximum displacement response spectrum 41

Figure 6.2: Br. 27568 midspan displacement estimate, 90 mph moving load 42

Figure 6.3: Br. 27568 midspan displacement estimate range, 20 mph moving load 42

LIST OF TABLES

Table 4.1: Natural frequencies (Hz) for clean and noisy model..... 33

Table 4.2: Acceleration and displacement error for variously damped systems 33

Table 4.3: True modal properties of blind case study system 33

Table 4.4: Identified modal properties of blind case study system..... 33

Table 5.1: I-35W Bridge displacement estimation event detection results 39

Table 6.1: Br. 27568 girder and deck properties 43

EXECUTIVE SUMMARY

The parallel northbound and southbound structures composing the I-35W Saint Anthony Falls Bridge were opened to traffic in 2008. Construction of the bridge incorporated a “smart bridge” system, equipped with instrumentation for monitoring the behavior of the structures. Since its opening, over 500 sensors have been collecting data to better understand the behavior of post-tensioned concrete box girder structures with the potential to impact future designs. Recent interest has been placed in using the 26 accelerometers installed on the bridge in a vibration-based structural health monitoring system, with the goal of allowing the Minnesota Department of Transportation (MnDOT) to clearly evaluate the performance of the structure. Given that natural frequency alone may not be sufficient to determine the health of the I-35W Saint Anthony Falls Bridge, a simpler parameter, vertical displacements, was believed to be better suited to evaluate the performance of the structure. However, vertical displacements are not easily measured on structures such as the I-35W Saint Anthony Falls Bridge.

Conventional displacement measurement methods typically require a fixed reference point. Because the bridge spans the Mississippi River, contact-based displacement measurement techniques requiring scaffolding are not feasible. Various non-contact measurement methods have been proposed in the past, however they still require a fixed reference point and can have high associated costs. To avoid the shortcomings of the conventional measurement options, this study focuses on using the currently installed accelerometers to estimate the vertical displacements of the bridge.

The proposed method focuses on using the currently installed accelerometers to not only identify the up-to-date modal parameters of the system but also uses the acceleration data within a Kalman filter framework to estimate the vertical deflections of the southbound structure. The method is adapted for an output-only application to the I-35W Saint Anthony Falls Bridge, which combines the output-only modal parameters extracted using NExT-ERA/DC in conjunction with the dual Kalman filter (DKF). To achieve accurate displacement estimates, the filter requires a tuning process.

Using the proposed estimation and tuning method, a ‘best guess’ at the dynamic displacements of the I-35W Saint Anthony Falls Bridge was selected based on engineering judgement. To track the displacements over time, a systematic procedure based on the displacement estimate Root Mean Square (RMS) was created to identify large-response events. Tracking the properties of the dynamic displacement events over time could serve as an indicator of bridge stiffness; however, the seasonal variation observed in the first four modes of the structure’s natural frequencies was not evident in the generated displacement estimates.

The dual Kalman filter approach captures only dynamic displacements and not any corresponding static displacement due to slow loading. Because of the high stiffness of the I-35W Saint Anthony Falls Bridge, traffic loading is experienced as a relatively slow process compared to the natural vibrations of the structure. Therefore, it is concluded that there is a large non-zero mean component of the displacement response that is not captured by the estimation technique. GPS was to be used in conjunction with the dual Kalman filter estimation technique to estimate the full non-zero mean displacement response; however, the stiffness of the bridge results in low-frequency displacements that are too small to be

captured by readily available GPS sensors. As such, it is recommended that vertical displacement estimation from acceleration measurements using a dual Kalman filter not be implemented further on the I-35W Saint Anthony Falls Bridge.

CHAPTER 1: INTRODUCTION

The goal of a vibration-based structural health monitoring system is to allow owners to clearly evaluate the performance of the structure. Given the variation in the modal parameters demonstrated in a previous work (Gaebler, Shield, and Linderman 2017), natural frequency alone may not be sufficient to determine the performance of the I-35W Saint Anthony Falls Bridge. Additionally, the concept of monitoring natural frequencies may seem sufficiently abstract, as not to attract the buy-in required for field deployment and application. As such, a simpler parameter, with an immediate physical meaning, may be better suited for such monitoring programs.

Displacement measurements are not only easily understood with an immediately applicable physical meaning, but they can be direct indicators of structural health as well as contain information useful to various engineering applications (Park, Sim, and Jung 2013). Vertical displacement is informative for monitoring the long-term serviceability and short-term behavior of bridge structures. As a performance measure, it is indicative of bridge stiffness and offers a more direct comparison with design calculations and maintenance guidelines. However, vertical displacements are not easily measured on structures such as the I-35W Saint Anthony Falls Bridge.

Conventional contact-based displacement measurement methods typically require a fixed reference point. Linear variable differential transformers (LVDTs) and linear potentiometers for vertical deflection measurement are often deployed via the use of expensive temporary scaffolding. Because the bridge spans the Mississippi River, displacement measurement techniques requiring scaffolding are not feasible. Other contact measurement devices that have been applied for displacement estimation include strain gauges. This technique is known to be sensitive to noise, and the current strain gauge setup is not applicable to the displacement estimation of the I-35W Saint Anthony Falls Bridge.

As an alternative to contact-based measurements, various non-contact measurement methods have been proposed. Laser Doppler vibrometry can be used to measure bridge deflection and vibrations (Nassif, Gindy, and Davis 2005) and image processing techniques can track target points on bridges to estimate dynamic deflection (Lee and Shinozuka 2006). However, the cost associated with each of these methods can be high, and they still require a fixed reference point. Global Positioning System (GPS) can provide real-time location measurements; however, the relatively low accuracy for such a stiff structure renders this form of measurement unusable.

In an attempt to avoid the shortcomings of the mentioned measurement options, a deflection estimation method using only accelerometers was studied and applied to the I-35W Saint Anthony Falls Bridge. Previous approaches based on integration of acceleration measurements have been prone to drift and were very sensitive to measurement noise (French et al. 2012). The proposed method focused on using the currently installed accelerometers to not only identify the up-to-date modal parameters of the system but also to use the acceleration data within a Kalman filter framework to estimate the vertical deflections of the southbound structure.

CHAPTER 2: BRIDGE DESCRIPTION AND INSTRUMENTATION

The I-35W Saint Anthony Falls Bridge, which opened to traffic on September 19, 2008, is made up of two separate structures: parallel northbound and southbound bridges. Figure 2.1 shows an elevation view of the bridge. Each structure consists of four spans, numbered in ascending order from south to north, with the main span (Span 2) crossing the Mississippi River. The first three spans are continuous, with the fourth span separated by an expansion joint. The main span was constructed using segmental precast construction while the other spans were cast-in-place. Each bridge is 90ft-4in (27.53m) wide and carries 5 lanes of traffic.

Over 500 sensors were installed on the bridge to investigate the structural behavior, including vibrating wire strain gages, thermistors, fiber optic sensors, resistance strain gages, linear potentiometers, accelerometers, and corrosion monitoring sensors. The monitoring system has been collecting data since the opening of the bridge in 2008. This large dataset represents a unique opportunity to investigate bridge behavior over multiple years, seasons, and conditions, with the underlying objective to develop structural health monitoring protocols using long-term data from an in-service structure.

This work is focused on vertical deflection estimation using acceleration measurements. Twenty-six Kistler 8310B2 accelerometers were deployed on the bridge, located on both the northbound and southbound structures. A majority (20) of the accelerometers were installed on the southbound structure and were mainly concentrated on the main span. Twelve accelerometers were permanently positioned along the centerline of both boxes at midspan of Spans 1, 2, and 3 on each structure. Fourteen additional moveable accelerometers were placed in the exterior box of the southbound structure. The moveable accelerometers were placed in the configuration shown in Figure 2.2 on May 11, 2010 and remained in that configuration throughout this project. All accelerometers were oriented vertically except for Acc 8 and Acc 10, which were oriented transversely.

Acceleration signals were passed through a low-pass filter with a cutoff frequency of 159 Hz, and then digitized to 16 bits at 1000 Hz. The digitized data was then passed through a low-pass Kaiser window filter with a cutoff frequency of 23 Hz and decimated to 100 Hz. The accelerometers have a range of ±2g, a frequency response of zero to 250 Hz (± 5%), and a noise density of 38 μg/√Hz. DC sensors, as opposed to AC sensors, were chosen with the intention of measuring static deflection of the structure. However, the typical ambient vibration signal amplitude of 10 mg, which is superimposed on the 1g DC signal, uses a small portion of the analog-to-digital conversion range. The resulting low signal-to-noise ratio makes this integration difficult (French et al. 2012).

Several outages of the southbound accelerometers have occurred, mainly due to communication loss caused by presumed lightning strikes. One accelerometer (SN 20607900) failed and was not recorded after February 6, 2013. A complete list of outages, including the northbound accelerometers and all other sensing systems, can be found in Appendix A.

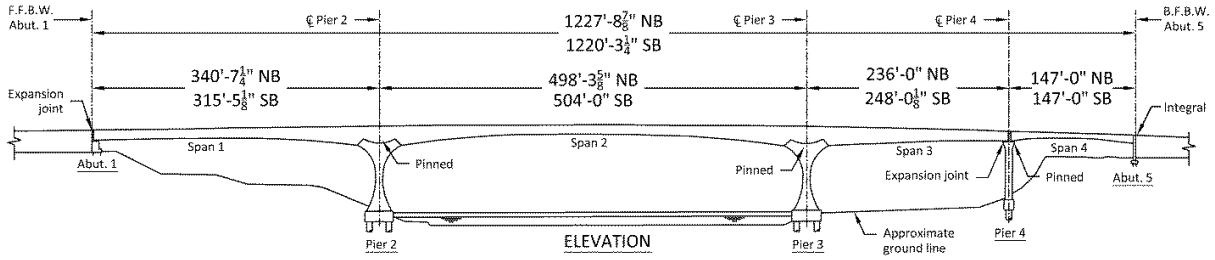

Figure 2.1: Elevation view of the I-35W Saint Anthony Falls Bridge (French et al. 2012)

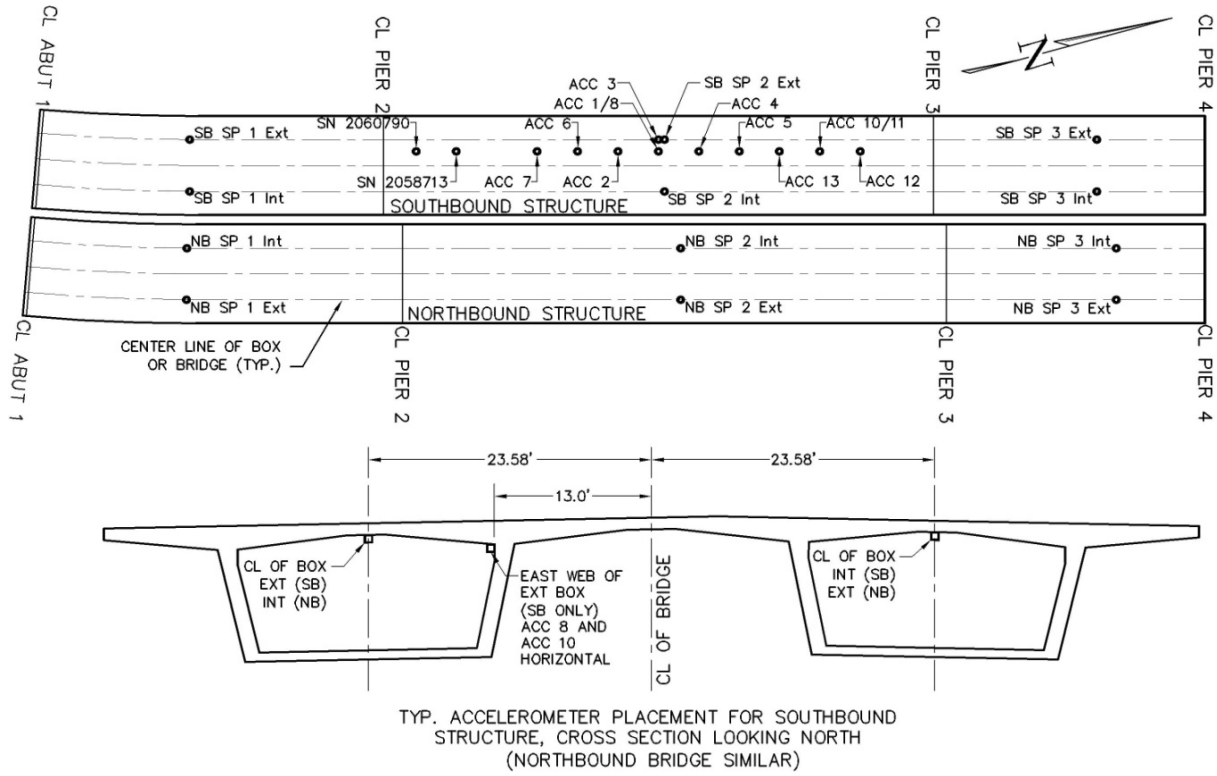

Figure 2.2: Long-term accelerometer layout used from May 11, 2010 until present (French et al. 2012)

CHAPTER 3: PREVIOUS MONITORING WORKS

The accelerometer data collected from the I-35W Saint Anthony Falls Bridge has been studied previously with the main intention of system identification. The modal parameters of the bridge, including natural frequency, mode shapes, and damping, were first identified from the accelerometer data by French et al. (2012). The identified natural frequencies were found to match closely with those obtained from the three-dimensional finite element model of the southbound structure, which was updated based on stiffness measured during static load tests. However, the structural mass in the finite element model could not be verified using the static measurements. The basic geometry of the finite element model as well as the predicted mode shapes of the first four modes are presented in Figure 3.1. The theoretical natural frequencies of the first four modes, using finite element analysis, were found to be 0.750 Hz, 1.464 Hz, 2.143 Hz, and 2.414 Hz, respectively (French et al. 2012).

Gaebler et al. (2017) analyzed all of the available accelerometer data for the southbound structure and studied how the modal parameters changed with temperature and time. The authors showed a seasonal variation in the identified natural frequencies of the structure (Figure 3.2) as well as a nonlinear correlation between natural frequency and temperature. In a long term vibration study on a reinforced concrete slab subjected to environmental temperature and humidity changes, Xia et al. (2006) found that mode shapes varied a relatively small amount compared to natural frequencies. This allowed Gaebler et al. to use a novel mode shape-based sorting technique to sort identification results of the I-35W Saint Anthony Falls Bridge. The first four mode shapes consistently identified by Gaebler et al. are shown in Figure 3.3, with yearly average natural frequencies of 0.817 Hz, 1.538 Hz, 2.273 Hz, and 2.352 Hz, respectively.

For both studies in which modal parameters were identified for the I-35W Saint Anthony Falls Bridge, system identification was performed using the Natural Excitation Technique (NExT) and the eigensystem realization algorithm with data correlations (ERA/DC). The NExT methodology, introduced by James III et al. (1993), is designed to estimate modal parameters of structures excited in their operating environment. The general idea of the technique is to use the auto- and cross-correlation functions, calculated from recorded vibration data, within a time-domain modal identification scheme as though the correlation functions were free vibration responses. The ERA/DC was the chosen modal identification scheme used within the NExT process. The eigensystem realization algorithm (ERA) was developed for modal parameter identification from test data in the time domain, and ERA using data correlations (ERA/DC) was introduced as an expansion of ERA in an effort to reduce bias errors due to noise corruption without the need for model overspecification (Juang and Pappa 1985; Juang, Cooper, and Wright 1988). ERA/DC was developed to use free response data, and it has been shown to be at least as accurate as ERA alone (Nayeri et al. 2009). When structures are under ambient excitations, free response data is generally not available, which is why the correlation functions are treated as free vibration responses in the NExT methodology. For a more complete description on the implementation of NExT-ERA/DC for the system identification of the I-35W Saint Anthony Falls Bridge, please refer to French et al. (2012) and Gaebler et al. (2017).

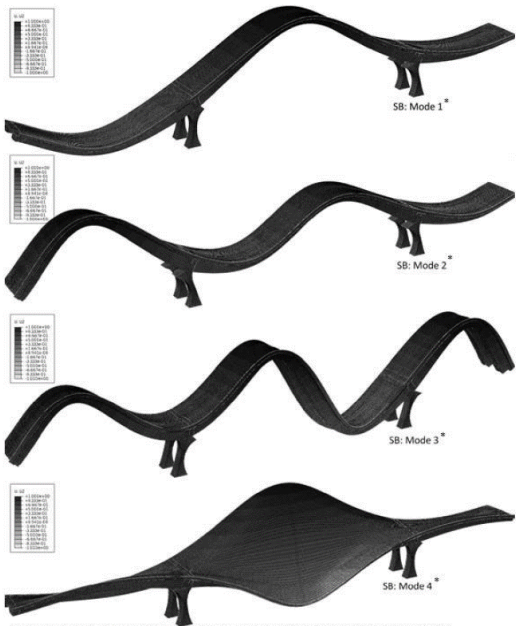

Figure 3.1: Southbound structure F.E.A. estimated mode shapes 1 through 4 (French et al. 2012)

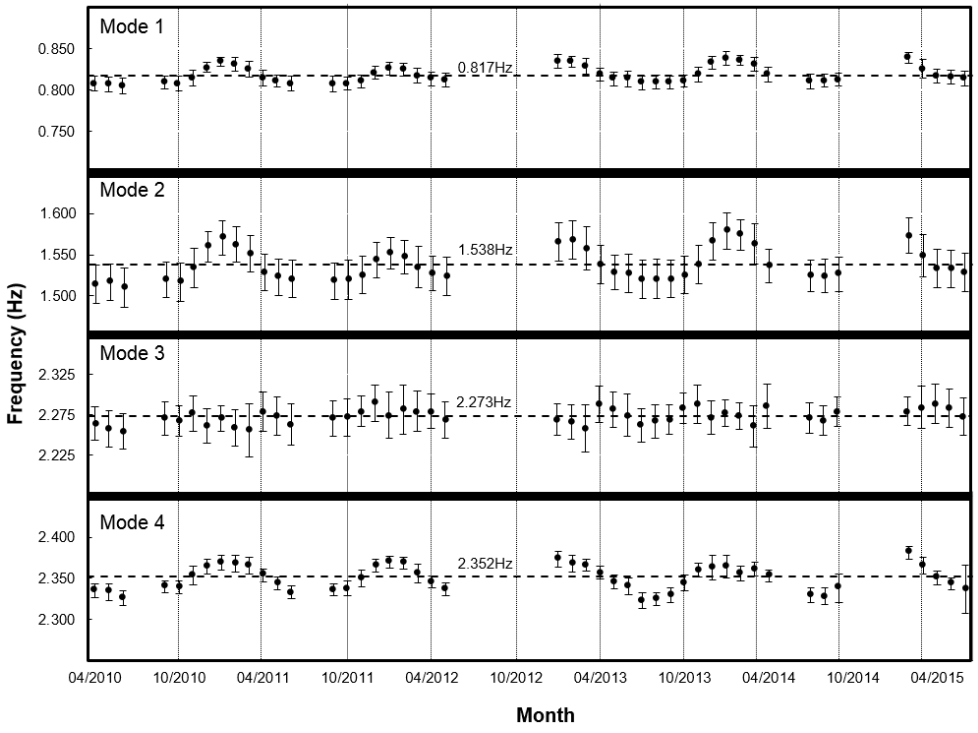

Figure 3.2: Monthly average natural frequency of modes 1 through 4 (Gaebler, Shield, and Linderman 2017)

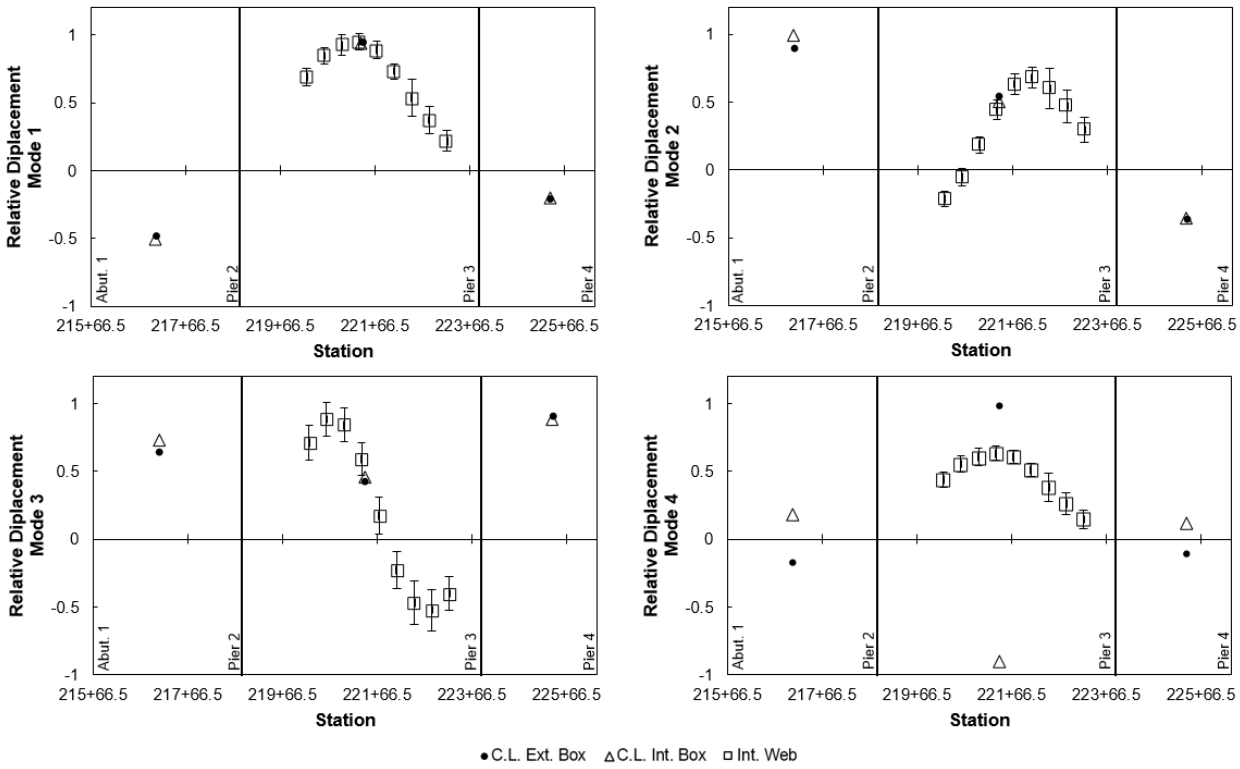

Figure 3.3: Southbound structure identified mode shapes 1 through 4 (Gaebler, Shield, and Linderman 2017)

CHAPTER 4: DISPLACEMENT ESTIMATION USING THE KALMAN FILTER

Given the benefits associated with the ability to monitor the displacement of a structure, as well as the difficulty in doing so directly, an indirect method of estimating displacement from recorded acceleration time histories would be beneficial. One such technique, which has been extensively studied, is the Kalman filter (Kalman 1960). The Kalman filter is a model-based technique, utilizing a dynamic model of the system to predict the corresponding state response (i.e., velocity and displacement) at certain locations given a time history of the measured output (i.e., acceleration).

As the technique is model-based, a system model is required. Typically, the system model is extracted from finite element software; however, there is no guarantee that such a model is in fact representative of the true system. To account for the unknown error in the system model, real-time and explicit model updating is often utilized to attempt to match the model response to the measured system response. Even with model updating, it is never possible to exactly model the system, and as such model noise will always be a source of error in the state estimations. Additionally, models of complex structures can become very large and cumbersome to use. For instance, the two-dimensional finite element model of the I-35W Saint Anthony Falls Bridge has over 30,000 nodes with over 90,000 degrees of freedom. Given that there are 20 accelerometers on the southbound structure, and thus 20 degrees of freedom currently monitored, a 90,000 degree of freedom model is impractical.

As opposed to utilizing available finite element models, an output-only Kalman filter technique that combines the output-only modal parameters extracted using NExT-ERA/DC in conjunction with the Kalman filter was used to estimate deflections. This output-only Kalman filter technique eliminated the complications associated with the large FE model, as well as the need for explicit model updating to ensure model accuracy.

Over the course of this project, two different Kalman filter estimation methods were considered. The first method was a single Kalman filter for state estimation only. The feasibility of the method was demonstrated on an experimental one-story, scaled building model as well as a two-dimensional ABAQUS model of the I-35W Saint Anthony Falls Bridge (Gaebler 2017). When the proposed technique was implemented on a small-scale laboratory test, it was found that the single Kalman filter was not well suited to estimate sudden displacement changes due to large changes in loading. This was due to the violation of an assumption required for use of the single Kalman filter on the type of loading that the structure experiences, which was assumed to be random with zero mean. It is possible that such an assumption may hold when considering loading on the I-35W Saint Anthony Falls Bridge, but there is no way to know for certain. To remove the assumption on the type of unknown excitation, a second Kalman filter was used to estimate the driving forces of the system. The act of estimating both input loading and displacements is known as joint input-state estimation; where in the present case it was performed using dual Kalman filters. Compared to a single Kalman filter estimation technique, the dual Kalman filter provided increased performance under excitation conditions that violate the assumed random, zero-mean input.

The dual Kalman filter (DKF) works in two separate stages; (1) a Kalman filter is used to estimate loads and (2) a separate Kalman filter is used to estimate displacements. Associated with each of the estimation systems is a certain level of process noise and acceleration measurement noise, which significantly affect displacement estimates. Specifically, the ratio of process noise to measurement noise serves as a single tuning parameter for each of the two estimation systems. These two ratios are representative of the amount of trust placed in the dynamic model, as compared to the trust in acceleration measurements. If the true ratios of process noise to measurement noise were known for the two estimation systems, they could be used to generate optimal displacement estimates. However, the two noise ratios are generally not known, and they must be tuned to provide acceptable estimates.

Because the modal output from NExT-ERA is used to define a model at the accelerometer locations only, and not at every point along the bridge, load estimates generated from the DKF end up being a set of equivalent forces acting at the accelerometer locations. Also, without knowledge of the exact bridge mass and its distribution, load estimates are scaled versions of the loading. Even considering that load estimates are a set of scaled, equivalent loads acting at the locations of the accelerometers, they may contain useful information about changes in traffic patterns or traffic loading if tracked over long periods of time.

The remaining portions of this chapter first detail the formulation of the model equations used to implement the dual Kalman filter. Then, the process of tuning the dual Kalman filter is explored via a simulated system, and a blind case study is considered to test the tuning applicability to the I-35W Saint Anthony Falls Bridge. Finally, there is a discussion on the advantages of using the dual Kalman filter when the input estimates are not of interest.

4.1 SYSTEM MODEL EQUATIONS AND THE DUAL KALMAN FILTER

In this section, a stochastic state-space representation of a discrete system is formulated for the implementation of the dual Kalman filter using an output-only system model. First, the equations of motion are used to generate the model and measurement equations of a discretized system in state-space form. Unlike other formulations, the equations are modified to account for an output-only implementation with unknown mass. Finally, the discrete-time equations are supplemented with stochastic noise vectors and the dual Kalman filter algorithm is introduced to jointly estimate both inputs and states.

4.1.1 State-Space System Equations

Consider the equations of motion for a discretized system

$$\mathbf{M}\ddot{\mathbf{u}}(t) + \mathbf{C}\dot{\mathbf{u}}(t) + \mathbf{K}\mathbf{u}(t) = \mathbf{f}(t) = \mathbf{S}_{\mathrm{p}}\mathbf{p}(t) \tag{1}$$

where $\mathbf{u}(t) \in \mathbb{R}^n$ is a displacement vector, $\mathbf{M}$, $\mathbf{C}$, and $\mathbf{K} \in \mathbb{R}^{n \times n}$ represent the mass, damping, and stiffness matrix, respectively, and $\mathbf{f}(t) \in \mathbb{R}^n$ is the excitation force vector. A single dot and double dot

over a vector denote first and second time derivatives, respectively. The force vector can be represented as a superposition of p input time histories $\mathbf{p}(t) \in \mathbb{R}^p$ modified by an influence matrix $\mathbf{S}_\mathrm{p} \in \mathbb{R}^{n \times p}$.

When using output-only system identification methods, it is convenient to formulate the problem in modal coordinates. The undamped eigenvalue problem corresponding to Eq. (1) is written:

$$\mathbf{K}\boldsymbol{\Phi} = \mathbf{M}\boldsymbol{\Phi}\boldsymbol{\Omega}^2 \tag{2}$$

where the solution gives the mode shapes and natural frequencies of the system. Introducing the coordinate transformation:

$$\mathbf{u}(t) = \boldsymbol{\Phi}\mathbf{z}(t) \tag{3}$$

where $\mathbf{z}(t) \in \mathbb{R}^n$ and premultiplying Eq. (1) by $\boldsymbol{\Phi}^T$, the equation of motion is rewritten in modal coordinates as:

$$\boldsymbol{\Phi}^\mathrm{T}\mathbf{M}\boldsymbol{\Phi}\ddot{\mathbf{z}}(t) + \boldsymbol{\Phi}^\mathrm{T}\mathbf{C}\boldsymbol{\Phi}\dot{\mathbf{z}}(t) + \boldsymbol{\Phi}^\mathrm{T}\mathbf{K}\boldsymbol{\Phi}\mathbf{z}(t) = \boldsymbol{\Phi}^\mathrm{T}\mathbf{S}_\mathrm{p}\mathbf{p}(t) \tag{4}$$

A limited number of vibration modes typically dominates the dynamic response of civil structures, and therefore a limited number of modes are identifiable by output-only methods. A truncated modal space could be substituted in Eq. (3) such that the modal matrix $\boldsymbol{\Phi} \in \mathbb{R}^{n \times m}$ consists of the m mode shapes as columns, where $m < n$, and $\mathbf{z}(t) \in \mathbb{R}^m$. Assuming proportional damping and that the orthogonality property of the mode shapes holds ($\boldsymbol{\Phi}^\mathrm{T}\mathbf{M}\boldsymbol{\Phi}$ is diagonal), Eq. (4) can be premultiplied by $(\boldsymbol{\Phi}^\mathrm{T}\mathbf{M}\boldsymbol{\Phi})^{-1}$ to arrive at a set of m decoupled equations:

$$\ddot{\mathbf{z}}(t) + \boldsymbol{\Gamma}\dot{\mathbf{z}}(t) + \boldsymbol{\Omega}^2\mathbf{z}(t) = (\boldsymbol{\Phi}^\mathrm{T}\mathbf{M}\boldsymbol{\Phi})^{-1}\boldsymbol{\Phi}^\mathrm{T}\mathbf{S}_\mathrm{p}\mathbf{p}(t) \tag{5}$$

where $\boldsymbol{\Omega} \in \mathbb{R}^{m \times m}$ is a diagonal matrix which contains the natural frequencies ω_i $(i = 1, \dots, m)$ in radians per second and $\boldsymbol{\Gamma} \in \mathbb{R}^{m \times m}$ contains entries of the form $2\zeta_i\omega_i$ on the diagonal, where ζ_i denotes the modal damping ratio.

By introducing the state vector $\mathbf{x}(t) \in \mathbb{R}^s$ where $s = 2m$ stands for the number of states, Eq. (5) can be represented as a continuous-time state equation:

$$\dot{\mathbf{x}}(t) = \mathbf{A}_\mathrm{c}\mathbf{x}(t) + \mathbf{B}_\mathrm{c}\mathbf{p}(t), \qquad \mathbf{x}(t) = \begin{bmatrix}\mathbf{z}(t) \\ \dot{\mathbf{z}}(t)\end{bmatrix} \tag{6}$$

with system matrices:

$$\mathbf{A}_{\mathrm{c}} = \begin{bmatrix} \mathbf{0} & \mathbf{I} \\ -\boldsymbol{\Omega}^2 & -\boldsymbol{\Gamma} \end{bmatrix}, \qquad \mathbf{B}_{\mathrm{c}} = \begin{bmatrix} \mathbf{0} \\ (\boldsymbol{\Phi}^{\mathrm{T}}\mathbf{M}\boldsymbol{\Phi})^{-1}\boldsymbol{\Phi}^{T}\mathbf{S}_{\mathrm{p}} \end{bmatrix}$$

We assume that only acceleration measurements are available, and that the measurement locations define the degrees of freedom of the discrete system. The acceleration measurement vector $\mathbf{y}(t) \in \mathbb{R}^n$ is expressed in terms of the state and input using the equation of motion to arrive at a state-space measurement equation:

$$\mathbf{y}(t) = \mathbf{C}_{\mathrm{c}}\mathbf{x}(t) + \mathbf{D}_{\mathrm{c}}\mathbf{p}(t) \tag{7}$$

where the output influence matrix and direct transmission matrix are:

$$\mathbf{C}_{\mathrm{c}} = [-\boldsymbol{\Phi}\boldsymbol{\Omega}^2 \quad -\boldsymbol{\Phi}\boldsymbol{\Gamma}], \qquad \mathbf{D}_{\mathrm{c}} = \left[\boldsymbol{\Phi}(\boldsymbol{\Phi}^{\mathrm{T}}\mathbf{M}\boldsymbol{\Phi})^{-1}\boldsymbol{\Phi}^{\mathrm{T}}\mathbf{S}_{\mathrm{p}}\right]$$

4.1.2 Output-Only Implementation

When using output-only models, $\mathbf{M}$ is generally unknown. In such a situation, mass normalization of mode shapes is impossible and an approximation on the system matrices $\mathbf{B}_{\mathrm{c}}$ and $\mathbf{D}_{\mathrm{c}}$ is required. The accuracy of the approximation with respect to the real system dictates whether the input estimates hold physical meaning. In the case that the approximation accurately reflects the physical system, $\mathbf{p}(t)$ represents force time histories and the loading on the structure. When the positions of the applied forces are unknown, the inputs become a set of equivalent forces acting at arbitrarily chosen points which would produce the same measured response (Lourens, Papadimitriou, et al. 2012). A more likely scenario is an inaccurate approximation of the system matrices, in which case the input estimates lose physical meaning. In order to satisfy Eq. (7) for a given acceleration measurement and state, $\mathbf{p}(t)$ must absorb the inaccuracies associated with the approximation made on $\mathbf{D}_{\mathrm{c}}$.

In this study, $(\boldsymbol{\Phi}^{\mathrm{T}}\mathbf{M}\boldsymbol{\Phi})^{-1}$ was assumed to equal the identity matrix of appropriate dimension and mode shapes were normalized such that the maximum relative displacement was one. The continuous time state space equations are:

$$\dot{\mathbf{x}} = \mathbf{A}_{\mathrm{c}}\mathbf{x}(t) + \mathbf{B}_{\mathrm{p}}\mathbf{p}(t) \tag{8}$$

$$\mathbf{y}(t) = \mathbf{C}_{\mathrm{c}}\mathbf{x}(t) + \mathbf{D}_{\mathrm{p}}\mathbf{p}(t)$$

$$\mathbf{A}_{\mathrm{c}} = \begin{bmatrix} \mathbf{0} & \mathbf{I} \\ -\boldsymbol{\Omega}^2 & -\boldsymbol{\Gamma} \end{bmatrix}, \qquad B_p = \begin{bmatrix} \mathbf{0} \\ \boldsymbol{\Phi}^{\mathrm{T}}\mathbf{S}_{\mathrm{p}} \end{bmatrix}, \qquad \mathbf{C}_{\mathrm{c}} = [-\boldsymbol{\Phi}\boldsymbol{\Omega}^2 \quad -\boldsymbol{\Phi}\boldsymbol{\Gamma}], \qquad \mathbf{D}_{\mathrm{p}} = \left[\boldsymbol{\Phi}\boldsymbol{\Phi}^{\mathrm{T}}\mathbf{S}_{\mathrm{p}}\right]$$

4.1.3 Discrete-Time Stochastic State-Space Equations

For use with stochastic estimation approaches, the continuous time state space equations are represented in discrete time with appropriate noise. Eq. (8) can be implemented in discrete time with a

sampling rate $1/\Delta t$ such that discrete time instants are defined by $t_k = k\,\Delta t$, for $k = 1, 2, \ldots, N_t$. Under the assumption of a zero-order hold on the input, the discrete-time state-space equations are:

$$\begin{aligned} \mathbf{x}_{k+1} &= \mathbf{A}\mathbf{x}_k + \mathbf{B}\mathbf{p}_k \\ \mathbf{y}_k &= \mathbf{C}\mathbf{x}_k + \mathbf{D}\mathbf{p}_k \end{aligned} \tag{9}$$

where $\mathbf{A} = \exp(\mathbf{A}_\mathrm{c}\Delta t)$, $B = [\mathbf{A}_\mathrm{c} - \mathbf{I}]\mathbf{A}_\mathrm{c}^{-1}\mathbf{B}_\mathrm{p}$, $\mathbf{C} = \mathbf{C}_\mathrm{c}$, and $\mathbf{D} = \mathbf{D}_\mathrm{p}$. Eq. (9) is represented stochastically with the addition of process noise $\mathbf{w}_k^\mathrm{x} \in \mathbb{R}^s$ and measurement noise $\mathbf{v}_\mathrm{k} \in \mathbb{R}^n$ vectors:

$$\begin{aligned} \mathbf{x}_{k+1} &= \mathbf{A}\mathbf{x}_k + \mathbf{B}\mathbf{p}_k + \mathbf{w}_k^\mathrm{x} \\ \mathbf{y}_k &= \mathbf{C}\mathbf{x}_k + \mathbf{D}\mathbf{p}_k + \mathbf{v}_k \end{aligned} \tag{10}$$

The process noise and measurement noise vectors are assumed to be uncorrelated, zero-mean, white noise signals with covariance matrices $\mathbf{Q}^\mathrm{x} \in \mathbb{R}^{s\times s}$ and $\mathbf{R} \in \mathbb{R}^{n\times n}$, respectively.

4.1.4 Dual Kalman Filter for Input and State Estimation

The dual Kalman filter (DKF) can be used to estimate the unknown input $\mathbf{p}_k$ and state $\mathbf{x}_k$ of the Eq. (10) system using the noisy acceleration measurements $\mathbf{y}_k$. The DKF scheme is divided into two stages: a Kalman filter to estimate the input and a Kalman filter to estimate the system state. Input estimation is accomplished by introducing a fictitious process equation that serves to propagate the input forward in time:

$$\mathbf{p}_{k+1} = \mathbf{p}_k + \mathbf{w}_k^\mathrm{p} \tag{11}$$

where $\mathbf{w}_k^\mathrm{p} \in \mathbb{R}^p$ is an assumed zero-mean, white process noise with covariance matrix $\mathbf{Q}^\mathrm{p} \in \mathbb{R}^{p\times p}$. A detailed explanation of the DKF and complete filter equations can be found in Appendix B.

4.2 TUNING THE DUAL KALMAN FILTER

In the following sections, examples of a simulated system are explored to highlight the process of tuning the dual Kalman filter for displacement estimates. Tuning refers to proper selection of the noise covariance matrices $\mathbf{Q}^\mathrm{x}$, $\mathbf{Q}^\mathrm{p}$, and $\mathbf{R}$ to achieve accurate estimates of the unobserved state and input. Since measurements are necessary to operate the DKF, it is usually possible to quantify the measurement noise covariance $\mathbf{R}$ prior to implementing the filter. In tuning the other noise covariance matrices, we will assume the covariance matrices of the input noise and process noise take the form $\mathbf{Q}^\mathrm{p} = Q^p \times \mathbf{I}$ and $\mathbf{Q}^\mathrm{x} = Q^x \times \mathbf{I}$, where Q^p and Q^x are scalar quantities. Such an assumption is typical when no information on the cross-correlation of the noise elements is available (Franklin, Powell, and Workman 1998). The magnitudes of Q^p and Q^x are the variances of the noise components.

Because the accuracy of the estimates can only be judged if the true state and input are known, estimated quantities will be compared to the simulation excitation and response to gain insight on the effects of tuning. To simplify this comparison, a steady-state form of the DKF algorithm presented by Azam, Chatzi, and Papadimitriou (2015) is used for estimation. Due to the formulation of the input estimator, numerical instabilities arose when trying to solve for the steady state gains prior to implementing the filter. Therefore, the time-varying DKF was run until steady state was reached, and then a time-invariant DKF was applied to the entire time history using the steady state gains. The time-invariant filter allowed for comparison of the entire response and estimate time histories without having to take the learning time of the filter into consideration.

4.2.1 Simulated System

For the discussion on tuning the dual Kalman filter, a simulated 8 degree of freedom (DOF) system is considered. The system is a series of masses connected to each other with identical spring/damper couplings, with the first and last masses connected with the same coupling to fixed supports as shown in Figure 4.1. Each node has a mass of $1\ \mathrm{lb}\ (0.45\ \mathrm{kg})$ and the stiffness between each mass is $200\ \mathrm{lbf/ft}\ (2919\ \mathrm{N/m})$. The modal damping ratio of each mode varied depending on the case under consideration but is set at 2% for the initial discussion.

The implementation of the dual Kalman filter was based on the simulated measurements generated by subjecting the system to a spatially correlated white noise excitation at each node. For each node, the same white noise signal was randomly shifted in time, with an average lag of 0.1 seconds. This excitation was used to approximate the correlated input at different nodes expected in a civil structure. The full system response was simulated in discrete time with a sampling rate of 100 Hz. Acceleration time histories from each node were used as measurements in the DKF, with varying amounts of Gaussian noise added to simulate measurement noise.

4.2.2 Tuning $\mathbf{Q^x}$ and $\mathbf{Q^p}$

In most practical settings, the noise covariance matrices needed to implement the DKF are unknown. Several works in the literature provide rule-of-thumb methods to appropriately tune the filter; however, most authors assume prior knowledge of the process noise Q^x. In so doing, the covariance of the input noise Q^p acts as a single tuning parameter for the DKF, and L-curve-type approaches are often taken to select the input covariance Q^p (Lourens, Reynders, et al. 2012; Azam, Chatzi, and Papadimitriou 2015; Tatsis and Lourens 2016; Petersen et al. 2018). Such an assumption is difficult to make when constructing a model using output-only system identification results, where the amount of uncertainty in the model may be unknown. If no knowledge of the process noise covariance Q^x is known a-priori, it becomes a second tuning parameter of the system.

The dual Kalman filter algorithm is run for various combinations of Q^x and Q^p to estimate the response from the acceleration measurements using a model constructed from the modal parameters of the system. After the entire time history is estimated, two separate metrics are used to judge the performance of the DKF.

One metric looks at the norm of the estimation error for the measured quantities $\sum\|\mathbf{y}_k - (\mathbf{C}\mathbf{x}_k^- + \mathbf{D}\hat{\mathbf{p}}_k)\|_2^2 / N_t$ over the tunable range of Q^x and Q^p. This is analogous to the L-curve type approaches seen in other works, only expanded to also allow proper selection of the process noise covariance. Since it is assumed that all measured quantities are accelerations, this metric quantifies the error of the acceleration estimates. The tunable range for Q^x and Q^p is difficult to define prior to computing the estimates, however values larger than and smaller than the magnitude of the measurement noise covariance should be considered.

The second metric used to judge the performance of the estimator is focused on the accuracy of the unobserved displacement state estimates. In practice, this comparison is impossible as displacement measurements are assumed unavailable. For simulations, however, the exact displacement response is available and a comparison is possible. As a metric to compare the estimated displacements to the simulated displacements, the average root mean squared error over all degrees of freedom $\sum_n \left(\sqrt{\sum_k \left(\mathrm{x}_{\mathrm{k,act}} - \mathrm{x}_{\mathrm{k,est}}\right)^2 / N_t} \right) / n$ is adopted.

These two metrics, one to judge the accuracy of the acceleration measurements and one to judge the accuracy of the displacement estimates, are analyzed jointly to provide insight on how to tune for proper estimation of the unobserved displacement state from only knowledge of the acceleration error.

4.2.3 Tuning When No Noise is Present

The DKF algorithm was implemented using the true modal parameters within the system model and using acceleration measurements with no noise added (i.e. clean model, clean measurements). The filter algorithm was run assuming a measurement noise covariance of $\mathbf{R} = 10^{-7} \times \mathbf{I}$, and displacement estimates were generated over the range $Q^x = [10^{-20}, 10^{-5}]$ and $Q^p = [10^{-20}, 10^{0}]$. A selection of the generated displacement estimates at node 4 is shown in Figure 4.2, which shows the significant effect of tuning on the displacement estimates. Figure 4.3 shows the power spectrum of the displacement estimates of Figure 4.2. Some displacement estimates have considerably larger high frequency content, which depends on the assumed level of process noise and input noise.

To aid in determining the tuning parameters that produce the most accurate acceleration and displacement estimate, the two error metrics are plotted as surfaces over the range of Q^x and Q^p as shown in Figure 4.4(a) and Figure 4.4(b), respectively. The two axes of the horizontal plane represent the tuning parameters of the displacement and input force estimation systems. Increasing values of the input noise covariance and process noise covariance coincide with a relative increase in trust in the acceleration measurements. The lowest point on the displacement error surface (Figure 4.4(b)) locates the tuning parameters with which the best displacement estimates were generated. The difficulty lies in finding this point based solely on the acceleration error surface (Figure 4.4(a)) and estimated displacements (i.e. without knowledge of the exact displacements).

In keeping with an L-curve approach based on the acceleration error, an input noise covariance of $Q^p = 10^{-7}$ would be chosen intuitively from Figure 4.4(a). However, proper selection of Q^x would be difficult

as it does not appear to affect the acceleration error for certain values of Q^p. From the displacement error surface (Figure 4.4(b)), any process noise covariance less than $Q^x = 10^{-15}$ with $Q^p = 10^{-7}$ gives the best displacement estimate. For this case, the optimal tuning parameters suggest that when relatively less trust is placed in the input estimator, more accurate displacement estimates are achieved.

When the displacement error surface is unknown, a modified representation of the acceleration error surface is required to determine the appropriate tuning parameter set. Figure 4.4(b) shows several flat portions on the displacement error surface, which are highlighted with red outlines. The combination of tuning parameters contained within each of the flat regions yield the same displacement error, and thus gives the same displacement estimate. The flat regions from the displacement error surface are superimposed onto the acceleration error surface in Figure 4.4(a). These four flat regions can be roughly identified from the acceleration errors only, using a projection of the upper valley as a dividing region on the lower plane. The identification of these flat regions from acceleration error, in turn, can be used to locate a region in which tuning makes a difference on displacement estimates. Figure 4.5 shows the region of tuning parameters that generate all the possible displacement estimates (black), which is identified by the connecting lines of the four flat regions (red).

Given that the displacement measurements are not available, the range of possible displacement estimates generated (as seen in Figure 4.2) is inspected to select the proper tuning parameters (from the black region) that provide an estimate that is acceptable to the user. Of course, this requires user judgement on the true response of the structure, from which there should be some form of engineering backing. Examples of judgement traits could include overall magnitude of the time history peaks or frequency content of the estimates, compared to what would be expected for the structure under consideration. One may prefer displacement estimates that contain the largest peak magnitudes in the time history while remaining a relatively smooth signal.

For the case with a perfect system and perfect measurements, the tuning parameters giving the best displacement estimates also produced the lowest acceleration error. This behavior should be expected from an L-curve tuning procedure, assuming the optimal acceleration and displacement estimates are produced by the same tuning parameters. This assumption, however, may not be true in all scenarios and for all noise levels. As a test, various amounts of noise were added to both the system model and the acceleration measurements to see what effects, if any, they had on tuning for displacement estimates.

4.2.4 Tuning When Model Noise and Measurement Noise is Present

Imperfections were added to both the system model and the acceleration measurements to see what effects, if any, they had on tuning for optimal displacement estimates. Various levels of damping were also considered. For each scenario, the DKF algorithm was run assuming a measurement noise covariance of $\mathbf{R} = 10^{-7} \times \mathbf{I}$. Displacement estimates were generated over the range $Q^x = [10^{-20}, 10^{-5}]$ and $Q^p = [10^{-20}, 10^{0}]$, and the acceleration error and displacement error surfaces were analyzed in an attempt to correlate the displacement estimate quality with the acceleration estimate quality.

4.2.4.1 Model Noise – Natural Frequencies and Mode Shapes

Model noise was introduced using noisy natural frequencies and mode shapes in the development of the DKF equations. The level of noise under consideration, as illustrated in the Figure 4.6 mode shapes and Table 4.1 natural frequencies, was motivated by the variation seen in the system identification results of the I-35W Saint Anthony Falls Bridge (Gaebler, Shield, and Linderman 2017) over a three week period. The amount of noise added to the modal properties of the system made no difference in any aspect of the tuning procedure or estimate quality. The tuning surfaces appeared similar in shape and magnitude to those constructed with the true modal properties, and the best displacement estimates ($Q^x = 10^{-15}, Q^p = 10^{-6}$) were able to capture the true system response ($Acceleration\ Error = 3.604, Displacement\ Error = 0.0029$).

To simulate the seasonal variation in natural frequencies seen in Gaebler, Shield, and Linderman (2017), a noisier model was considered in which the assumed natural frequencies of the system were increased by 0.105 Hz from the noisy model and the noisy mode shapes were not changed. The tuning surfaces were nearly identical in shape and magnitude to those constructed with the noisy modal properties.

For the level of noise considered in this study, the noise in the natural frequency and mode shape identification did not affect tuning or the displacement estimates. The best displacement estimates were generated by the tuning parameters that also produced the best acceleration estimates.

4.2.4.2 Damping

The effect of damping on tuning for displacement estimates was considered in two manners: by varying the magnitude of the damping ratio over the range $0.5\% \leq \zeta \leq 10\%$ and by using a poor-quality damping identification estimate.

The response of the system was simulated for modal damping of 0.5%, 2%, and 10% and the tuning surfaces were generated assuming these damping values. Each scenario was under the same excitation, and therefore the magnitude of the response decreased with increased damping. Because the two error metrics are not normalized, the error values obtained for the three damping cases are not directly comparable. However, it was found that while different in magnitude, the shapes of the error surfaces were similar (2% case shown in Figure 4.4), and similar tuning values produced the best displacement estimates and acceleration estimates for all the trial damping values. Table 4.2 lists the tuning parameters which yielded the best displacement estimates and the corresponding error values for each of the three damping cases. While the values of Q^x vary somewhat in Table 4.2 for the different damping cases, they are all contained within the same flat region on the acceleration error surface and are thus similar selections. The system response was captured quite well by the estimator.

Poor damping identification was simulated by assuming 5% modal damping when the measurements were generated from a 2% modally damped system. The error surfaces were similar in shape to those where the assumed damping was correct, as were the tuning parameters yielding the lowest displacement error (Table 4.2). It seems that enough trust could be placed in the measurements

(relatively speaking) to overcome the poor damping estimate in the model so that the system response could be accurately estimated by the DKF.

For the damping cases considered in this study, it was found that (1) for the range of damping values typically exhibited by large structures, similar tuning values produce the same relative quality of displacement estimate and (2) good displacement estimates can still be recovered using poor identification results assuming the measurements are of sufficient quality. Also, the best displacement estimates were generated by the tuning parameters that also produced the best acceleration estimates.

4.2.4.3 Model Truncation

As the development of the DKF lends itself well to model constructions using only a few modes, the effect of model truncation was considered by generating estimates using only the first four modes (2% damping). As would be expected, truncating the model diminishes the estimator's capability to capture the exact, full order response to a white noise excitation. Figure 4.7 shows a portion of the best displacement estimate time history for a truncated model with noisy modal parameters. Interestingly, the tuning values ($Q^x = 10^{-14}, Q^p = 10^{-7}$) which give the best displacement estimates ($Acceleration\ Error = 55.3, Displacement\ Error = 0.0059$) for the truncated model were similar to the best tuning parameters for the full order model ($Q^x = 10^{-16}, Q^p = 10^{-6}$). The shapes of the error surfaces were similar between the truncated and full order model, and the best acceleration estimates were produced by the tuning parameters that gave the best displacement estimates.

4.2.4.4 Measurement Noise

Measurement noise was introduced to the simulated acceleration responses for the 0.5%, 2%, and 10% damped systems by adding a zero-mean Gaussian noise. Various signal-to-noise ratios (SNR) were considered (SNR = 15, 20), simulating the noise levels which are seen in the accelerometer data obtained from the I-35W Saint Anthony Falls Bridge (French et al. 2012). The DKF was implemented assuming the true full order model with measurement noise covariance $\mathbf{R} = 10^{-7} \times \mathbf{I}$.

For both noise levels and all damping levels, the shape of the acceleration error surface was like all other cases, but the displacement error surface was different. Figure 4.8 shows the displacement error for the 2% damped system with measurement noise (SNR = 20). The surface is shown from a different perspective so the point with the minimum error is visible ($Q^x = 10^{-13}, Q^p = 10^{-12}$). A portion of the displacement estimate at node 4 produced by the minimum error tuning parameters is shown in Figure 4.9. Significantly poorer estimation performance is achieved when measurements are contaminated with noise ($Acceleration\ Error = 31.81, Displacement\ Error = 0.0080$). Dissimilar to all other forms of model noise considered, the minimum displacement estimates were not generated by the tuning parameters that produced the minimum error acceleration estimates.

4.2.5 Tuning Conclusions

When the noise covariance matrices needed to implement the DKF are unknown, an expanded L-curve type approach can be used to aid in tuning. The expanded approach incorporates both the process noise covariance and input noise covariance, and provides insight on the estimated measurement vector error. From this, a region can be defined in which tuning makes a difference on the state estimates.

Because the minimum error displacement estimates were not necessarily generated by the tuning parameters that produced the minimum error acceleration estimates when measurement noise was present, it is unlikely that one could select the optimal tuning parameters from the acceleration error surface only. Instead, the range of possible displacement estimates must be inspected to select the proper tuning parameters that provide an estimate that is acceptable. This requires engineering judgement on the true response of the structure.

From experimentation, the authors have noticed that the displacement estimates with the largest peaks, while remaining smooth, are often best. The tuning parameters corresponding to these best displacement estimates typically lie on the boundary of the region in which tuning makes a difference on the displacement estimates, as taken from the acceleration error surface.

4.3 BLIND CASE STUDY

To test the tuning procedure outlined in Section 4.2 for displacement estimation in a more realistic setting, a blind case study scenario was considered. The only information available to the individual who performed the study was (1) acceleration measurements, (2) geometry of the structure including sensor location, and (3) an approximation of the first 6 natural frequencies. In general, knowledge of the structure geometry and sensor location is not necessary to implement the DKF procedure, but they are usually known. Natural frequency approximations are typically available from finite element models and can be used as a check for output-only modal parameter identification.

The structure for the blind case study is shown in Figure 4.10 and was designed to roughly approximate a bridge with a flexible pier at midspan. It is a 20 ft $(6.1$ m$)$ long simply supported concrete beam ($w_c = 100$ lb/ft^3 $(15.7$ kN/m$^3)$, $f_c' = 5$ ksi $(34$ MPa$)$, $E_c = 4030.5$ ksi $(27996$ MPa$)$) with a vertical spring support ($k = 441.685$ kip/ft $(6445.91\ kN/m)$) at midspan. The rectangular cross section (2 ft wide by 6 ft deep $(0.61$ m $\times\ 1.83$ m$)$) was constant along the length of the beam. Table 4.3 shows the modal parameters of the simulated system. The simulated system was excited along the length by a spatially correlated band-limited white noise and the corresponding acceleration measurements provided contained measurement noise (SNR = 20).

NExT-ERA/DC (see Juang and Pappa 1985; Juang, Cooper, and Wright 1988; James III et al. 1993) was used to identify the modal parameters such as natural frequencies, mode shapes, and damping ratios of the unknown system from six separate simulated acceleration data files. For each run, the results were sorted by mode shape, and the identification result with the highest consistent-mode indicator (CMI) was kept (see Pappa, Elliott, and Schenk (1993)). Table 4.4 lists the averages of the identified parameters from the six runs that were used to formulate a model of the structure to be used in the dual Kalman

filter. The first, third, and fifth vibrational modes of the structure were identified using the output-only technique.

Figure 4.11 shows the acceleration error as a function of process noise and input noise covariances for an assumed $\mathbf{R} = \mathbf{I}$. The acceleration error provided little guidance in selecting the tuning parameters, so the displacement estimates themselves were assessed. Of the displacement estimates generated over the range of tuning parameters shown in Figure 4.11, Figure 4.12 displays a representative sample of the smoother estimate time histories. Displacement estimates with large amounts of drift or with frequency content higher than expected were discarded based on engineering judgement. The estimates in Figure 4.12 differ mainly by the magnitude of the peaks, and those with very low magnitudes have a slight phase shift.

The dashed line ($Q^x = 10^{-7},\ Q^p = 10^{-10},\ \mathbf{R} = \mathbf{I}$) is a smooth estimate (essentially no visible high frequency content) with peak magnitudes that encompass all other peaks. Towards the end of the acceleration record, this dashed estimate drifts slightly away from a noisier estimate with a true zero mean. If a truly smooth estimate without drift was desired, the dashed line could be used to estimate shorter segments of data, thus avoiding the drift that occurs after long periods of time. However, one must consider the effects of the filter initial conditions if taking such an approach. An estimate with similarly large peak amplitudes, but with a low level of high frequency content ($Q^x = 10,\ Q^p = 10^{-6}$, $\mathbf{R} = \mathbf{I}$) was selected instead of the dashed estimate as the authors 'best guess' for displacement estimation. Selecting the estimate with the largest magnitude was treated as a conservative approach, especially if large displacements are unfavorable. Figure 4.13 shows the input estimates at node 3 corresponding to the two displacement estimates previously mentioned ($Q^x = 10^{-7},\ Q^p = 10^{-10}$ and $Q^x = 10,\ Q^p = 10^{-6}$). In comparing the estimated inputs, it appears that the slight drift in the dashed displacement estimate is caused by significant drift in the corresponding input estimation.

The blind displacement estimates, generated by the tuning parameters ($Q^x = 10, Q^p = 10^{-6},\ \mathbf{R} = \mathbf{I}$), compared well to the simulated structural displacements. Figure 4.14 shows the estimated displacements compared to the true displacements at node 3 for a single run. In this case, good agreement is seen between the estimated and true displacements (node 3 RMSE = 0.0201 in $(0.511\ \text{mm})$). The results of the blind case study show that the tuning method can be used on structures where displacement measurements are not available.

4.4 ADVANTAGES OF THE DUAL KALMAN FILTER WHEN INPUTS ARE NOT OF INTEREST

In this work, the input estimator in the dual Kalman filter is used as a tool towards state estimation. Because the input estimates in this approach are not considered, one may question why it is necessary to have the second estimator. The main reason for its use is displacement estimation performance, especially under various loading types. When no input estimator is used, an approximation on the type of excitation is necessary. In situations where the approximation on the type of excitation would be incorrect, or where the input excitation is truly unknown, it can be advantageous to estimate the inputs using a second Kalman estimator. The increased performance of the dual Kalman filter over the single Kalman filter is explored via a simulated example and an experimental test.

4.4.1 Simulated Example

Consider state estimation of the 8 DOF system of Section 4.2 (2% damping) using a single Kalman filter (see Kalman (1960)). The estimation problem could be formulated using Eq. (10) and setting $\mathbf{B} = \mathbf{0}$ and $\mathbf{D} = \mathbf{0}$. Such a construction inherently assumes that the modal excitation is a zero mean white noise. However, as in Section 4.2, the structure is excited by the random white noise excitation at all nodes, but randomly shifted in time. For comparison of the two formulations, i.e. a single Kalman filter (with $\mathbf{B} = \mathbf{0}$ and $\mathbf{D} = \mathbf{0}$) and the dual Kalman filter, the modal parameters used in the dynamic models are exact, and there is no measurement noise.

Figure 4.15 shows a portion of the optimal displacement estimate time histories for the single Kalman and dual Kalman estimation methods for the system under random loading. The figure shows that the single Kalman estimates ($Displacement\ Error = 0.008211$) are not as accurate as the dual Kalman estimates ($Displacement\ Error = 0.001543$), but it does give reasonable displacement estimates for some portions of the time history. Note that the process noise covariance to give the optimal displacement estimate is not the same for the single Kalman estimator ($Q^x = 10^{-13}$) and dual Kalman estimator ($Q^x = 10^{-16}, Q^p = 10^{-7}$). Figure 4.16 shows the acceleration and displacement error for the single Kalman filter estimates as a function of Q^x. Even though the single Kalman filter can match the acceleration measurements to a high precision (increasing Q^x in Figure 4.16(a)), increased acceleration estimate accuracy does not necessarily improve the displacement estimates (Figure 4.16(b)). Higher accuracy is not achieved in the single Kalman filter displacement estimates by using a measurement noise covariance of $\mathbf{R} = 2.8657 \times \mathbf{I}$, i.e. the true covariance of the random excitation, as this places more distrust in the correct acceleration measurements.

While the single Kalman estimator performs comparably for the modified random excitation, it is not able to capture the initial displacement response in the case of an impulse loading, which is significantly different from the assumed excitation. An impulse time history with a single nonzero value of 1000 at $t = 1$ sec was applied to node 4 of the same 8-dof model described in Section 4.2 (2% damping). The system response was estimated using both the single and dual Kalman filter estimators. From the possible range of estimates, optimal displacement estimates were generated with the same noise covariances as for the random excitation case and are shown in Figure 4.17. Simply stated, the dual Kalman filter can react faster than the single Kalman filter to the acceleration measurements while remaining smooth. However, single Kalman filter displacement estimates are nearly identical to the dual Kalman filter estimates and the true displacement response about 1.1 seconds (110 measurements) after the impulse. Of course, the speed with which the single Kalman filter approaches the dual Kalman filter is dependent on the selection of Q^x and $\mathbf{R}$. As more trust is placed in the measurements, the initial spike in the single Kalman estimator increases in magnitude but corrects to the true value quicker.

4.4.2 Experimental Test

To verify the proposed Kalman filter estimation technique on a physical structure, a small-scale laboratory test was conducted in the Structures Laboratory at the University of Minnesota that compared displacements estimated using the Kalman filtering technique to displacements measured

using linear variable differential transformers (LVDTs). The laboratory test was performed on a single-story, single-bay steel frame with bolted connections. Figure 4.18 shows the experimental set up. An HSS 6x6x3/8 test beam was suspended between two W12x120 columns, and an isolated wooden frame was built beside the test frame as a reference platform for the contact-based displacement measurement sensors.

The test beam was subjected to an impact force, and the subsequent acceleration and displacement response was measured at eight locations along the beam. LVDTs measured displacements at the locations of the accelerometers. Figure 4.19 shows a schematic drawing of the experimental setup and sensor locations. At each sensing location, a PCB Piezotronics model 352C33 piezoelectric shear accelerometer (100 mV/g) and a $\pm$0.5" Schaevitz LVDT were fastened to an aluminum angle that was glued to the test beam. Figure 4.20 shows the accelerometer and LVDT attachment. Data was collected using an NI cDAQ-9178 and was sampled at 1600 Hz. The signals were passed through an elliptic low-pass filter with a 400 Hz cutoff frequency.

Displacements were estimated at the locations of the accelerometers using Kalman filter estimation techniques and were compared to the measured displacements. The dual Kalman filter was constructed using an output-only system identification procedure (NExT-ERA/DC) used in previous modal identification works and modified as in Section 4.1. Figure 4.21 shows the displacement estimation results at Location 4 (nearest midspan) from the single and dual Kalman filter approaches, as compared to the measured response. Like the simulated example, the dual Kalman filter is able to match the true displacement response due to an impact load faster than the single Kalman approach.

4.5 A SUMMARY OF DISPLACEMENT ESTIMATION USING A DUAL KALMAN FILTER

This work uses an output-only formulation of the dual Kalman filter for displacement estimation from noisy acceleration measurements. Unlike previous formulations that leverage model updating of an FEM model, only modal information from a typical output-only system identification is used. Without mass information, approximations must be taken in the formulation of the system equations that cause the input estimates to lose physical meaning. Even when the input estimates are not considered beyond their role in the filter, it was shown that the input estimator significantly increases state estimation performance under various loading types as compared to a single Kalman filter for state estimation.

The tuning process involves proper selection of two noise covariance parameters to achieve accurate estimates of the unobserved state and input. When the noise parameters are unknown, an expanded L-curve type approach can be used to aid in tuning. From information on the estimated measurement vector error, a region can be defined in which tuning makes a difference on the state estimates. While sources of model noise were found to have minimal impact on the selection of this region and the optimal tuning values, unknown measurement noise makes a significant impact.

Because of the presence of measurement noise, it is unlikely that one could select the optimal tuning parameters for state estimation from the expanded L-curve approach. Instead, this region of tuning values is used to generate a set of possible displacement estimates that must be inspected to select

tuning parameters that provide a reasonable and conservative state estimate, which requires engineering judgement on the true response of the structure. For example, the response characteristics of interest are the frequency content and magnitudes of the peak displacements. A simulated blind case study revealed that this identified region, along with engineering judgement, can be used to determine accurate displacement estimates despite using the simplified output-only based model of the system.

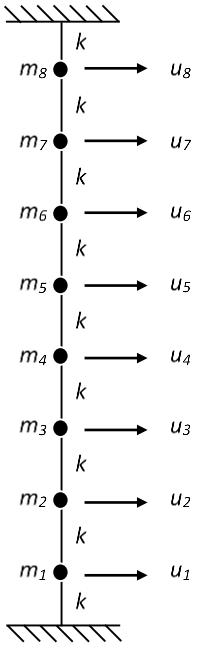

Figure 4.1: Simulated 8 degree of freedom system

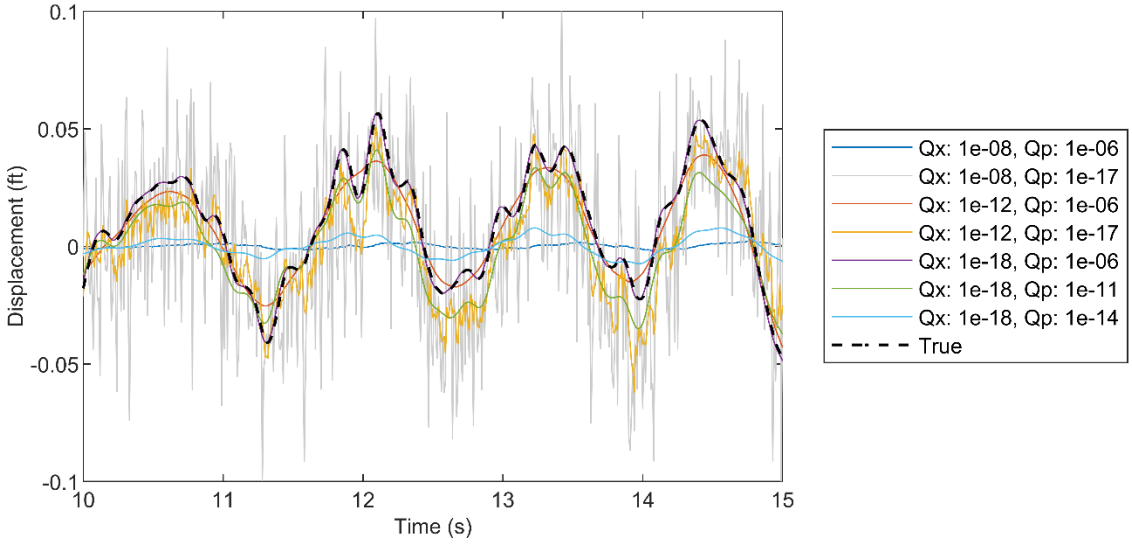

Figure 4.2: Displacement estimate range at node 4

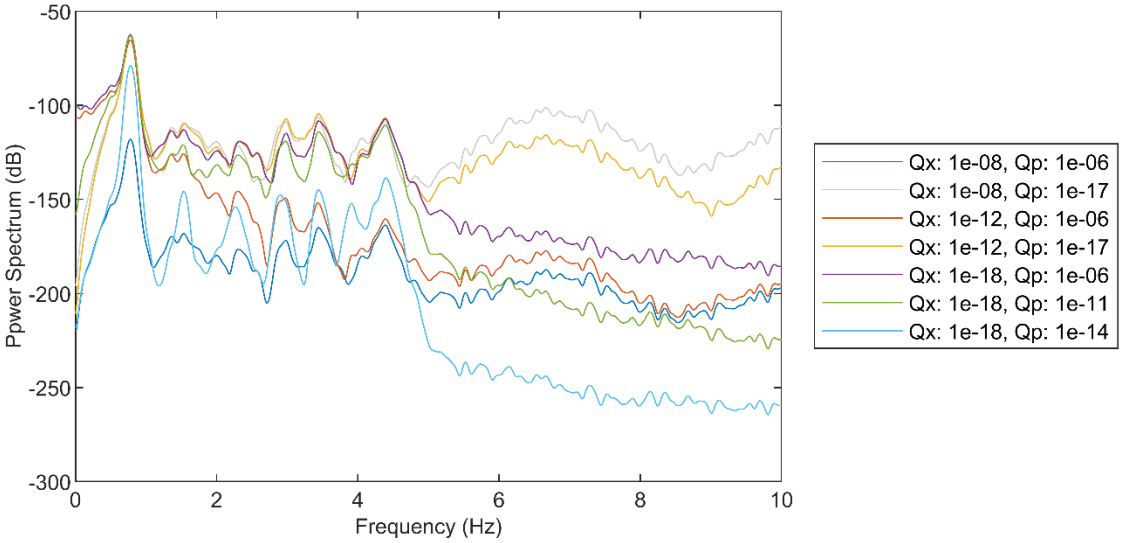

Figure 4.3: Power spectrum of displacement estimates

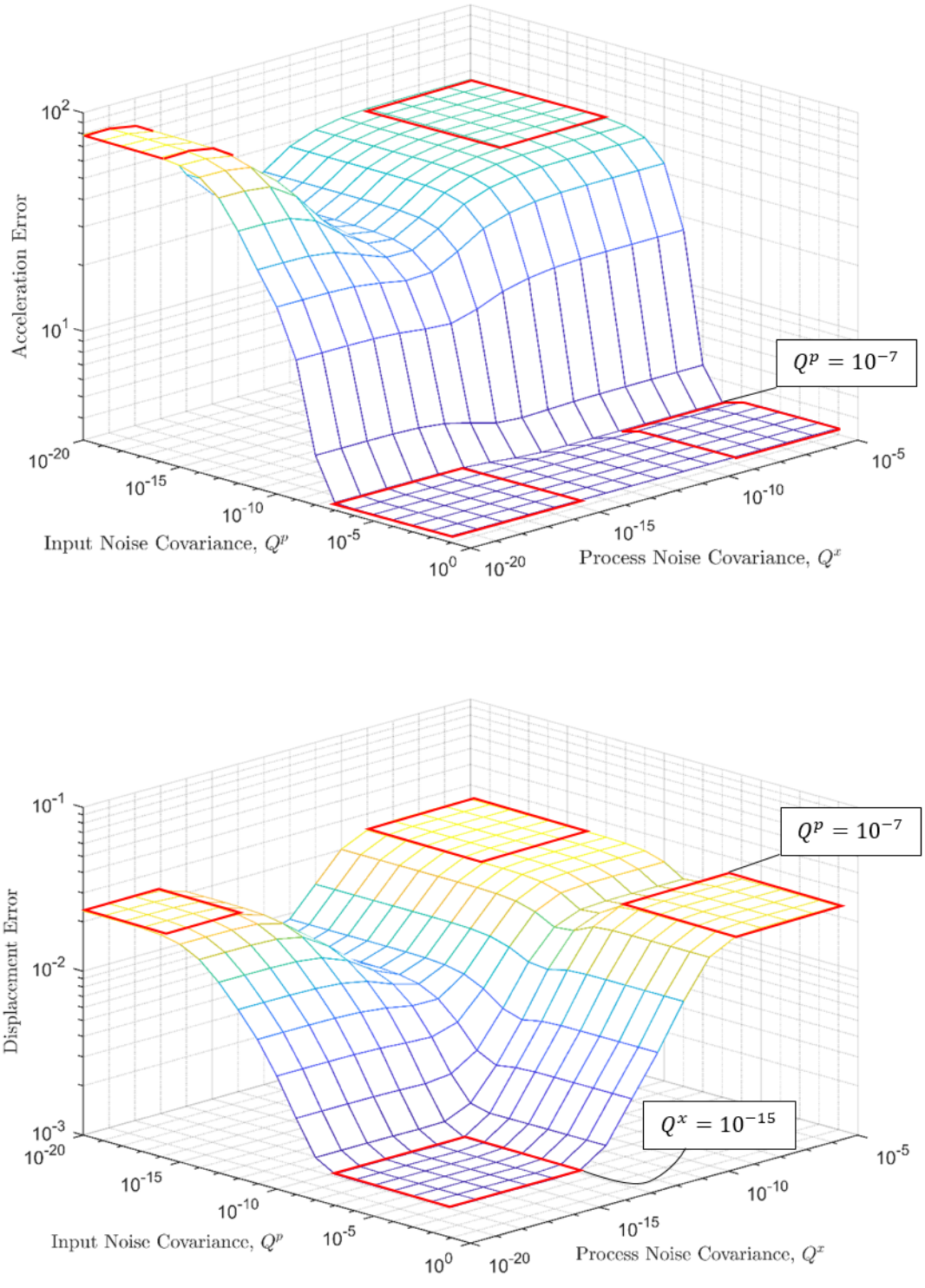

Figure 4.4: (a) Acceleration estimation error surface. Clean model, measurements. 2% damping. (b) Displacement estimation error surface. Clean model, measurements. 2% damping

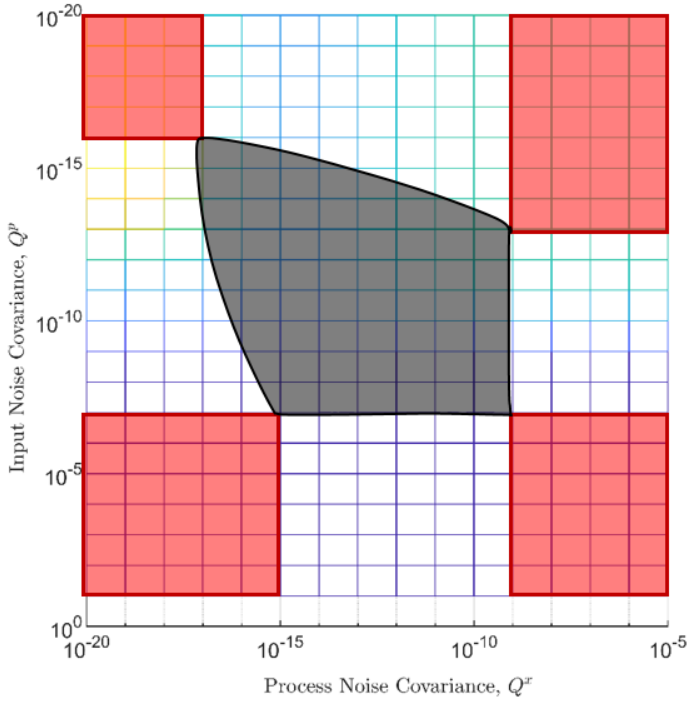

Figure 4.5: Top-down view of acceleration error surface. Flat regions (red) identify a region of tuning parameters that generate all possible displacement estimates (black)

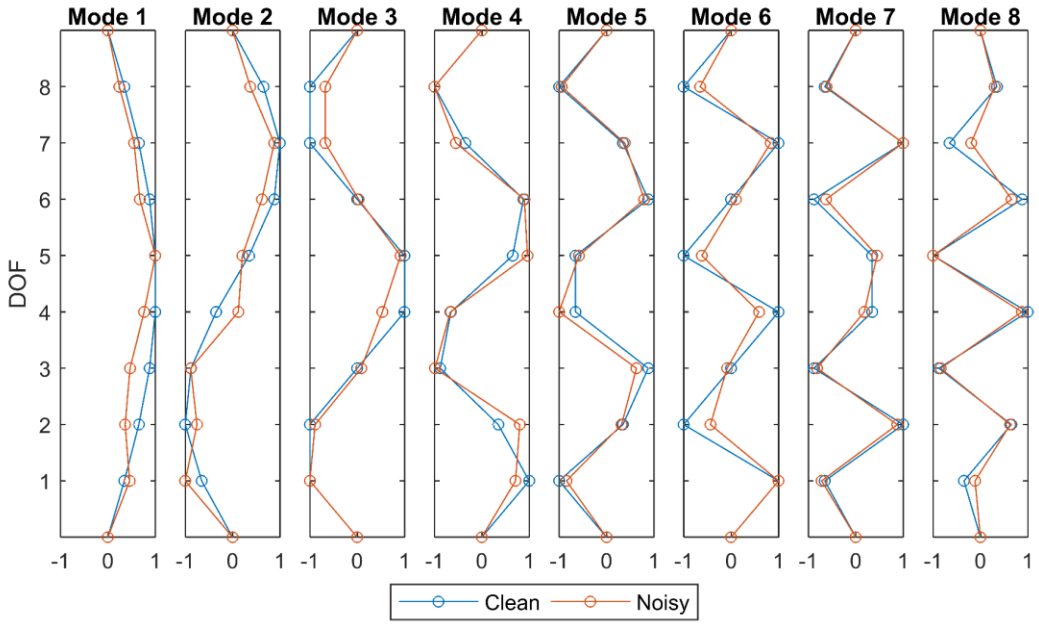

Figure 4.6: Mode shapes for clean and noisy model

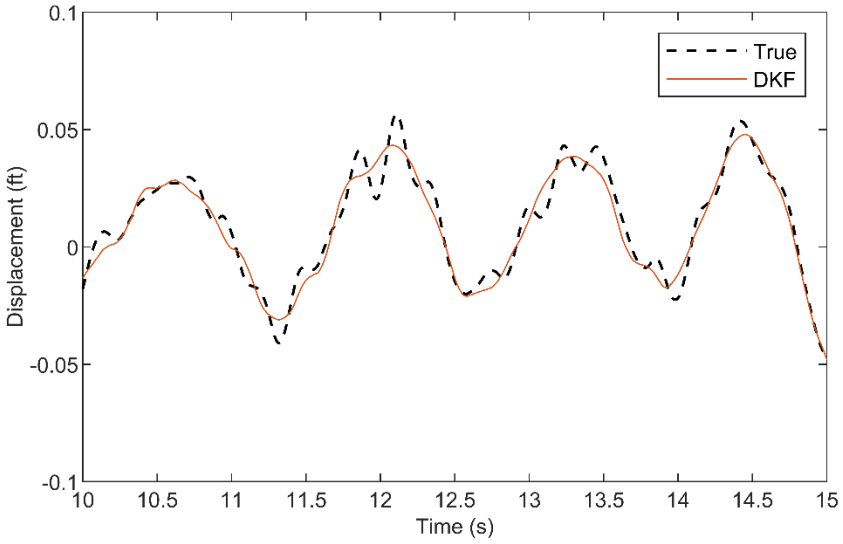

Figure 4.7: Displacement estimate using truncated model at node 4

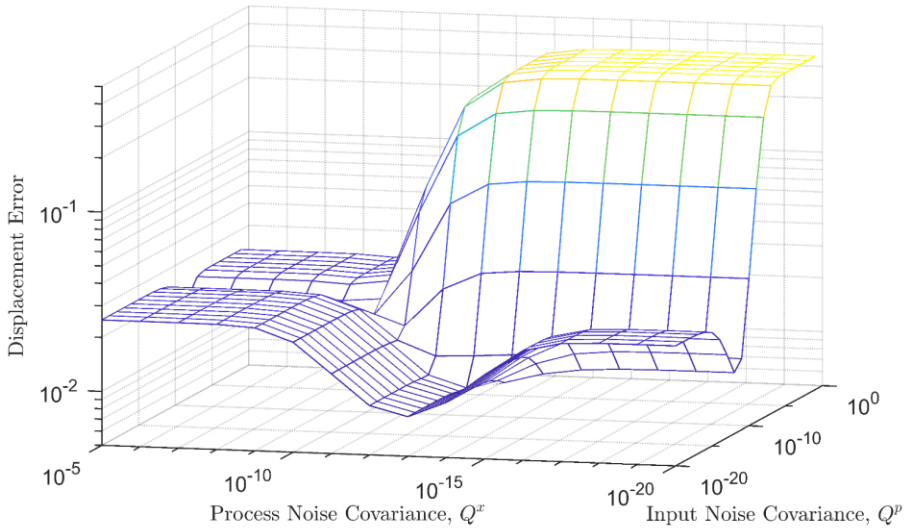

Figure 4.8: Displacement estimation error tuning surface. Clean model, noisy measurements (SNR = 20). 2% damping

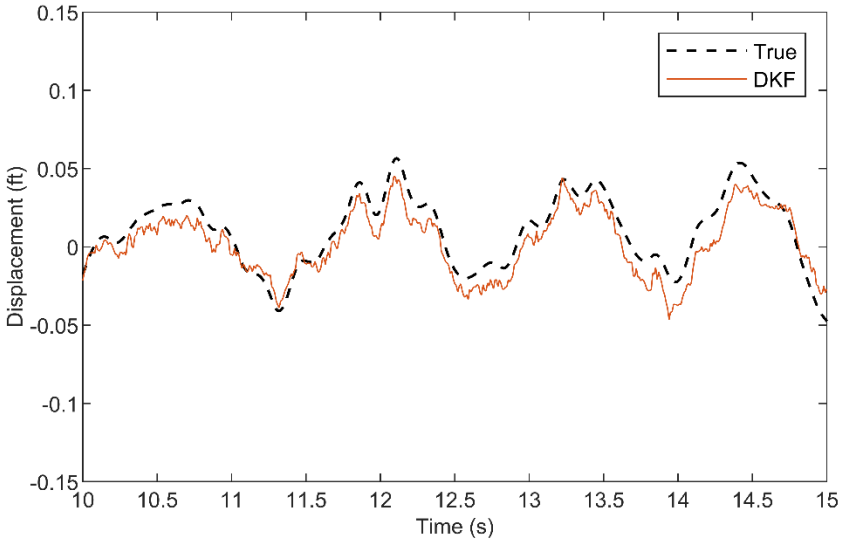

Figure 4.9: Displacement estimate at node 4 from noisy measurements (SNR = 20)

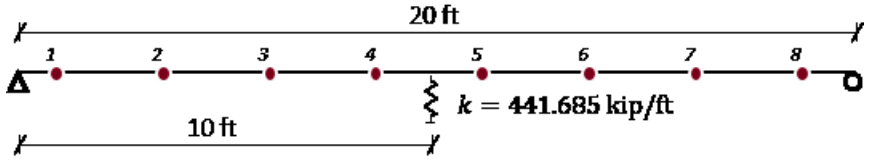

Figure 4.10: Blind case study system

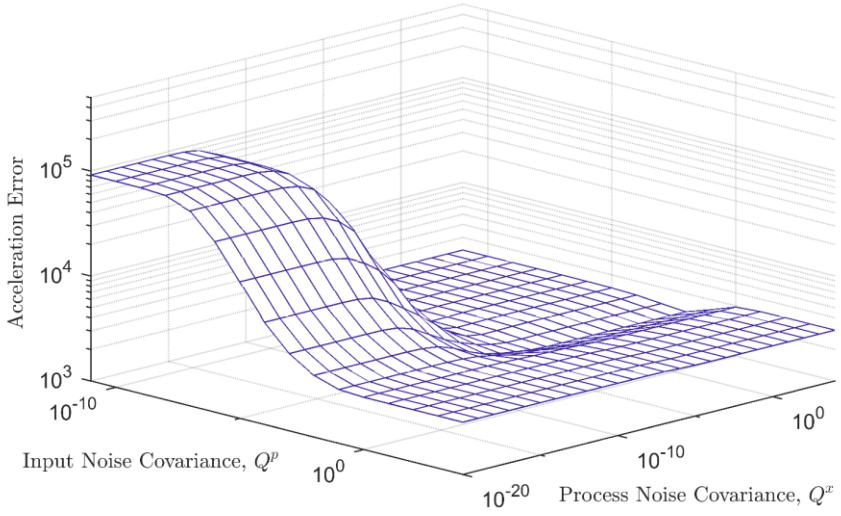

Figure 4.11: Acceleration estimation error surface for blind case study system

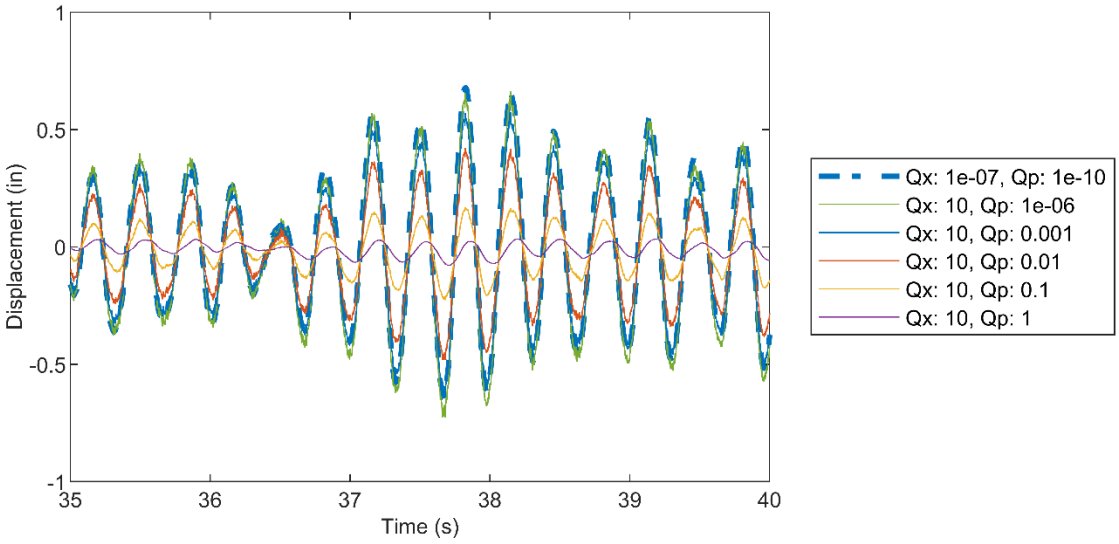

Figure 4.12: Displacement estimate range at node 3 for blind case study system

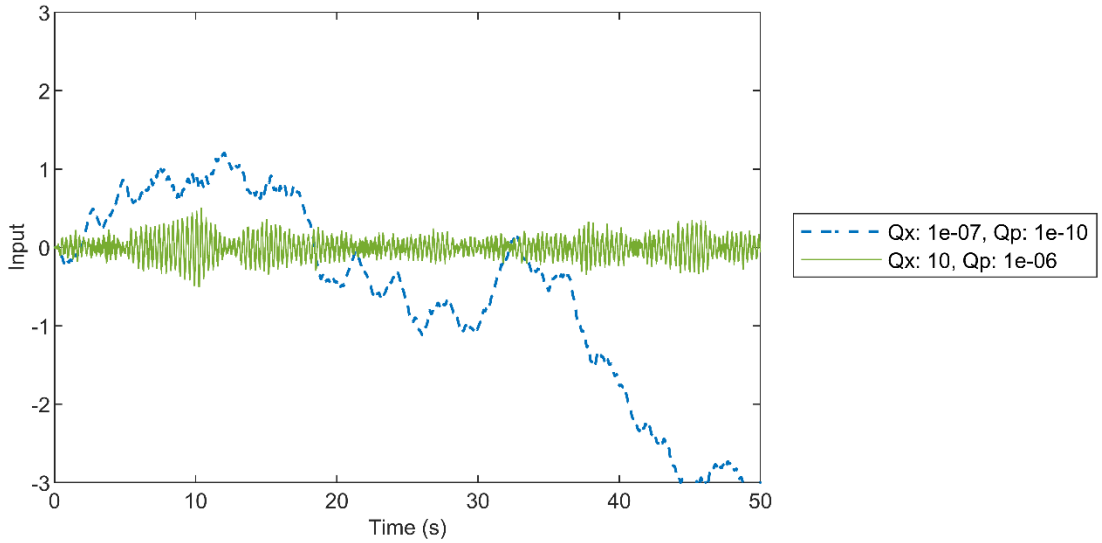

Figure 4.13: Input estimates at node 3 for blind case study system

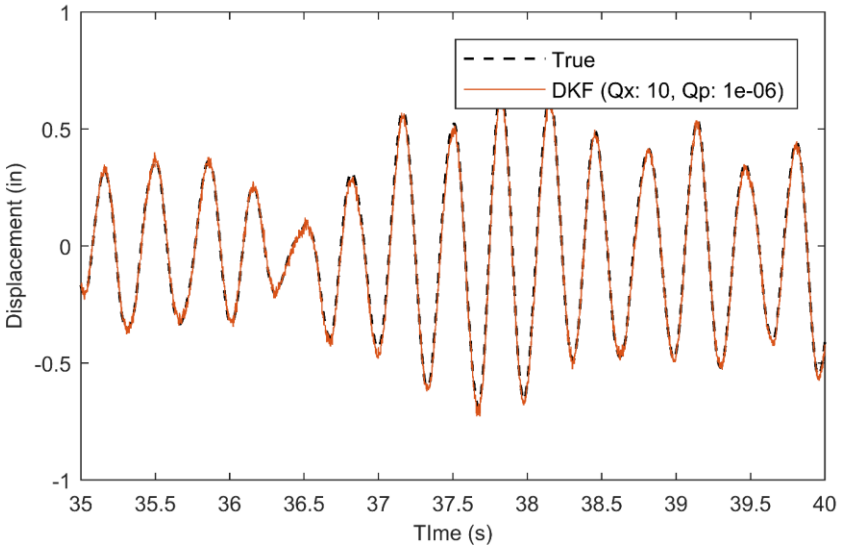

Figure 4.14: Comparison of displacement estimate from dual Kalman filter (DKF) for blind case study system at node 3

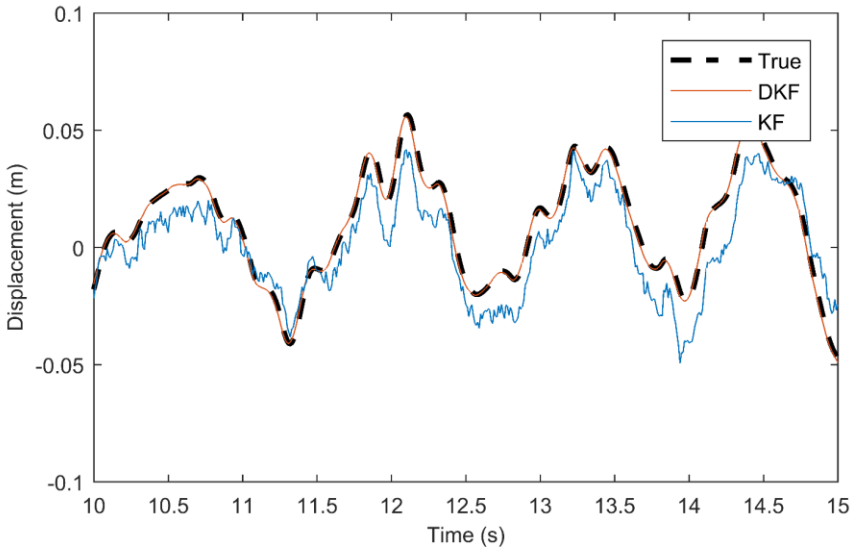

Figure 4.15: Displacement estimates from dual Kalman filter (DKF) and single Kalman filter (KF) at node 4, random excitation

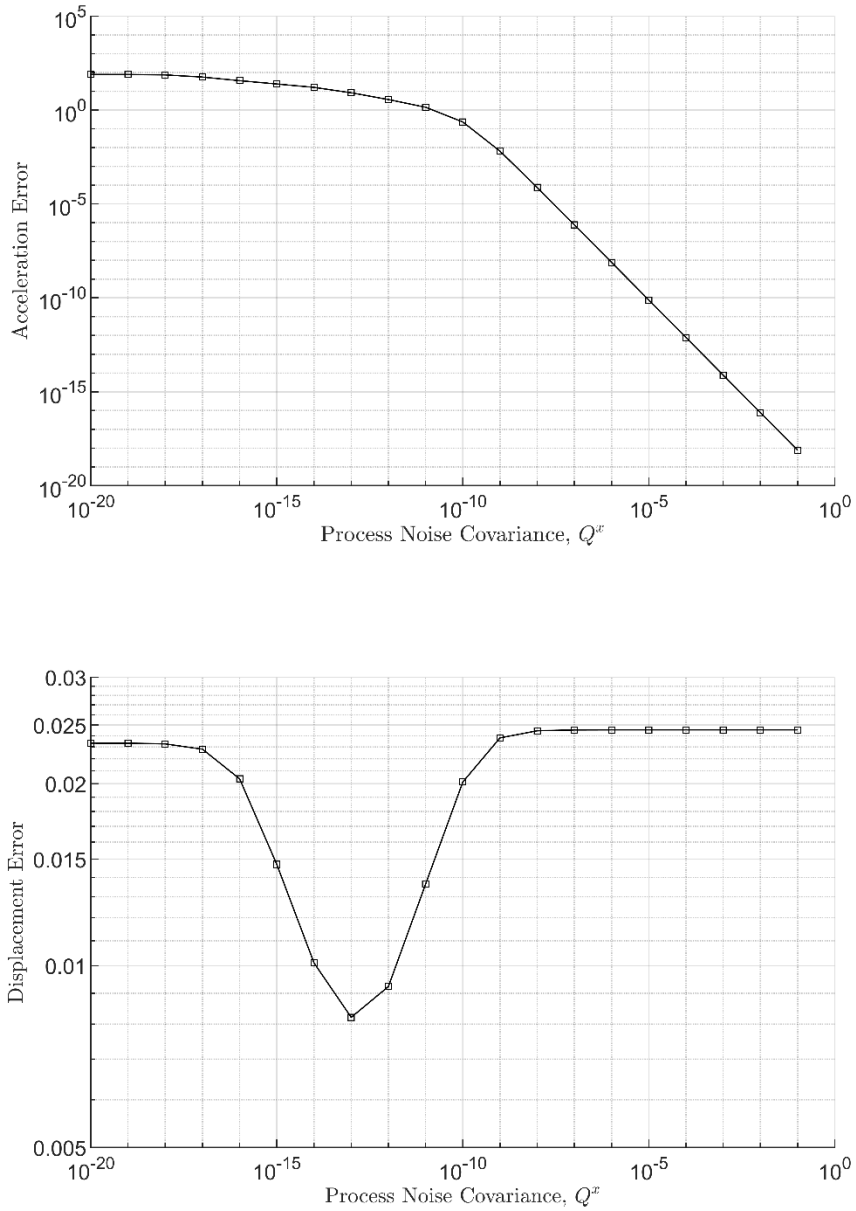

Figure 4.16: (a) Acceleration estimation error for single Kalman filter. Clean model, measurements. 2% damping, random excitation. (b) Displacement estimation error for single Kalman filter. Clean model, measurements. 2% damping, random excitation

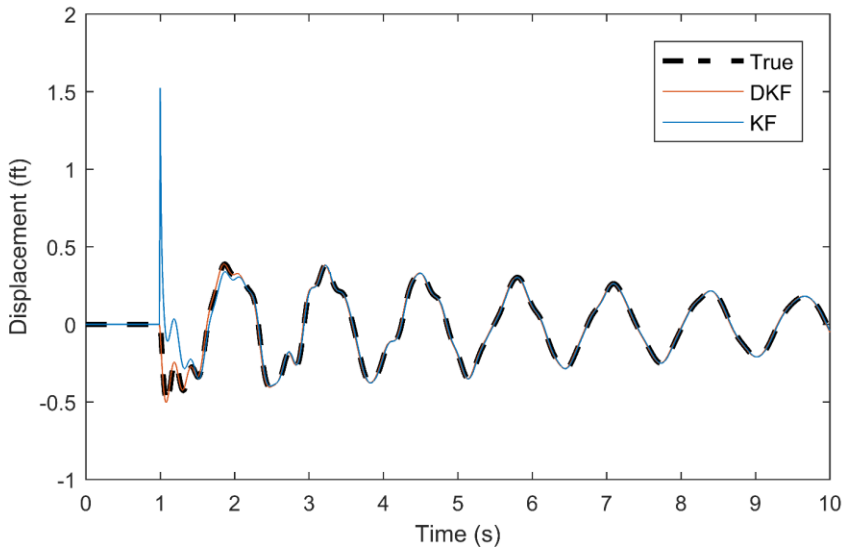

Figure 4.17: Displacement estimates from dual Kalman filter (DKF) and single Kalman filter (KF) at node 4 – impulse excitation

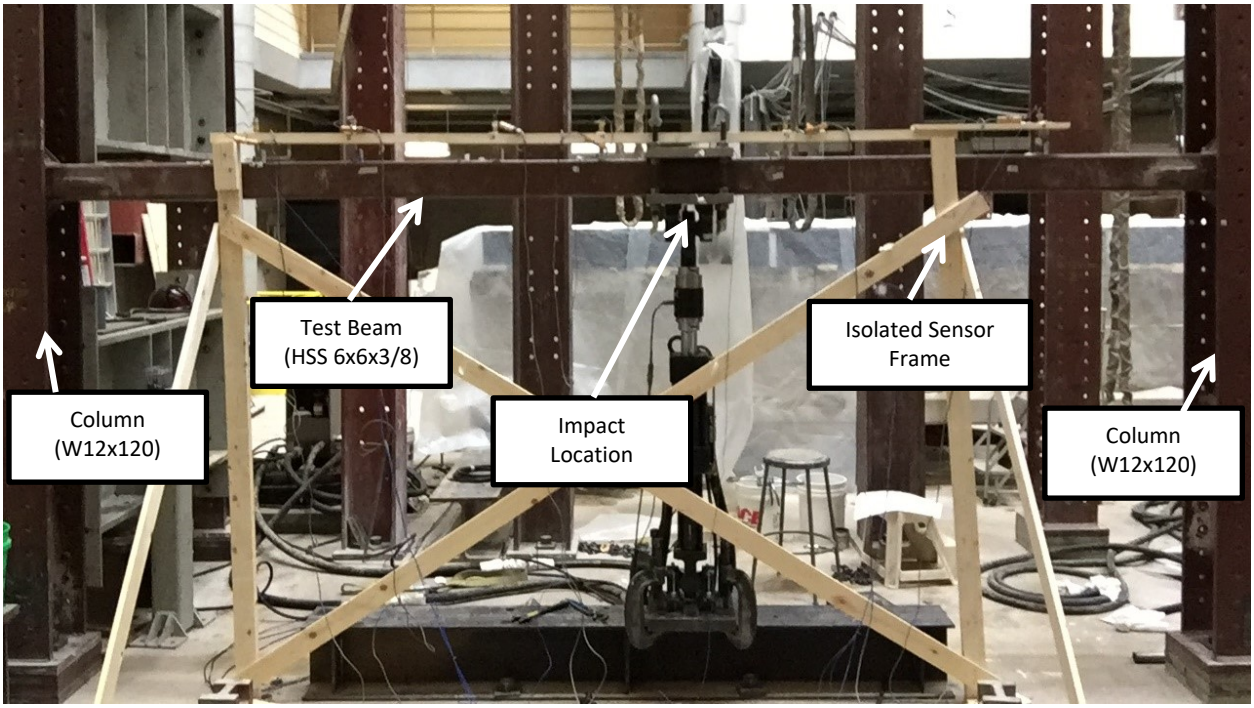

Figure 4.18: Laboratory experimental set up

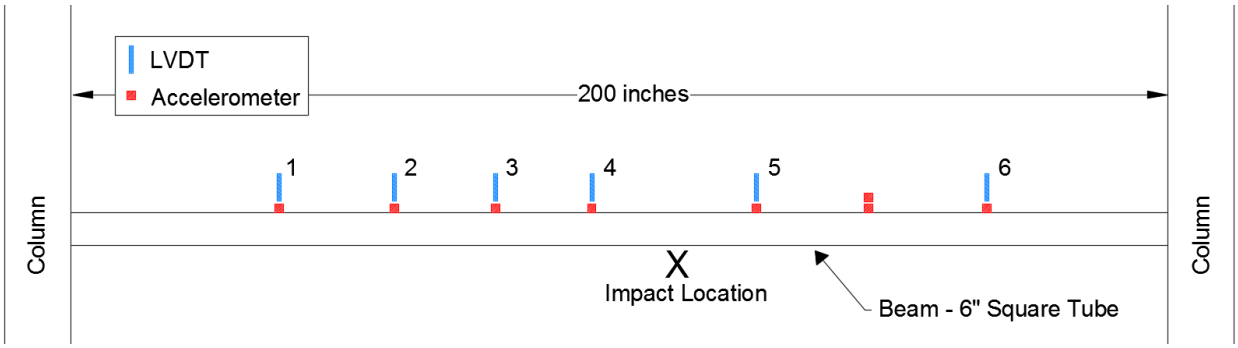

Figure 4.19: Schematic drawing of experimental setup and sensor locations

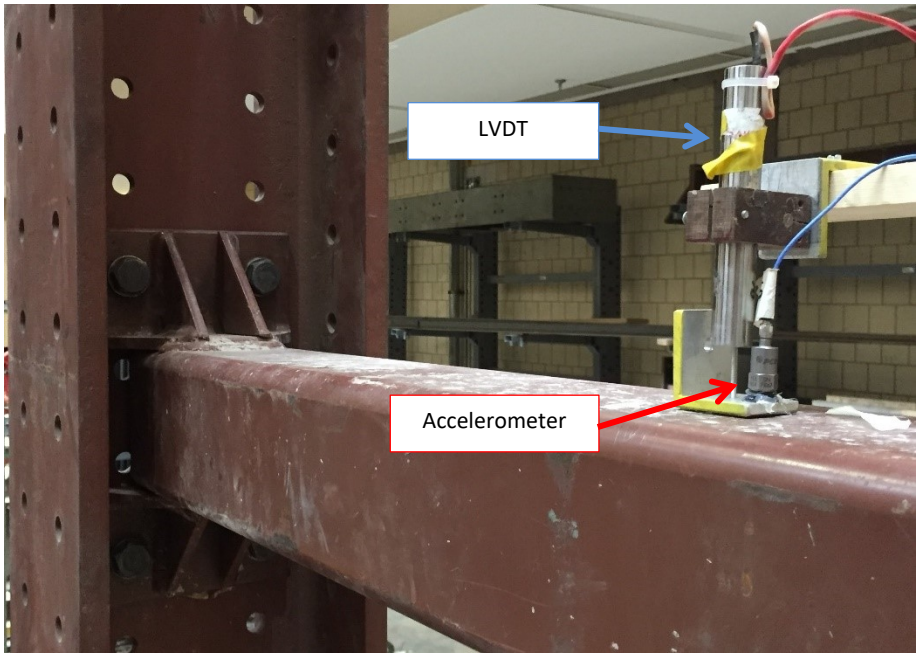

Figure 4.20: Beam-column connection with accelerometer and LVDT attachment

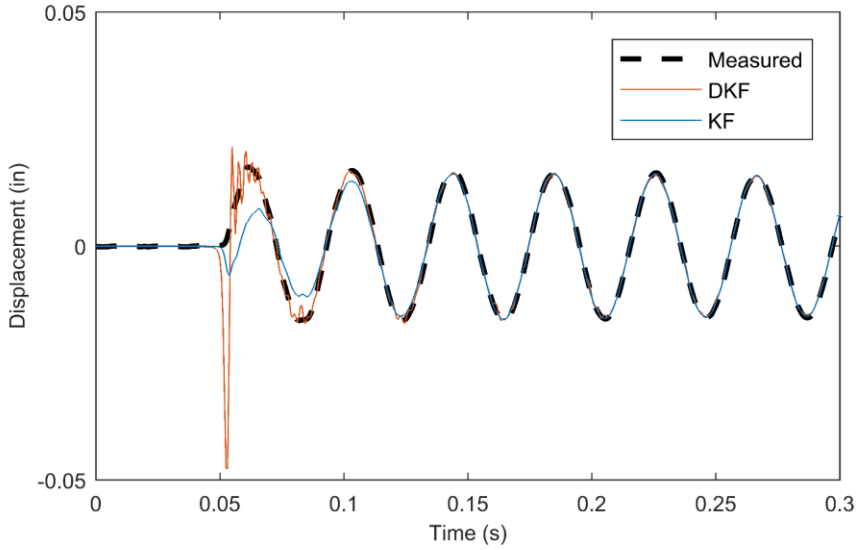

Figure 4.21: Displacement estimates from dual Kalman filter (DKF) and single Kalman filter (KF) at node 4 for experimental system

Table 4.1: Natural frequencies (Hz) for clean and noisy model

Mode	1	2	3	4	5	6	7	8
Clean	0.78	1.54	2.25	2.89	3.45	3.90	4.23	4.43
Noisy	0.77	1.56	2.28	2.87	3.45	3.91	4.21	4.38

Table 4.2: Acceleration and displacement error for variously damped systems

Damping		Parameters giving best displacement estimates		Error	
True	Assumed	Q^x	Q^p	Acceleration	Displacement
0.5%	0.5%	10^{-17}	10^{-6}	13.16	0.0029
2%	2%	10^{-16}	10^{-6}	3.398	0.0015
10%	10%	10^{-16}	10^{-6}	0.784	0.0007
2%	5%	10^{-15}	10^{-6}	3.592	0.0028

Table 4.3: True modal properties of blind case study system

Mode	Natural Frequency	Damping Ratio	Mode Shape							
[]	[Hz]	[]	dof 1	dof 2	dof 3	dof 4	dof 5	dof 6	dof 7	dof 8
1	3.06	0.02	0.35	0.65	0.88	1	1	0.88	0.65	0.35
2	4.46	0.025	0.65	1	0.88	0.35	-0.35	-0.88	-1	-0.65
3	9.89	0.03	1	1	0	-1	-1	0	1	1
4	17.84	0.031	1	0.35	-0.88	-0.65	0.65	0.88	-0.35	-1
5	27.90	0.04	1	-0.35	-0.88	0.65	0.65	-0.88	-0.35	1
6	40.14	0.06	1	-1	0	1	-1	0	1	-1

Table 4.4: Identified modal properties of blind case study system

Identified Mode	Natural Frequency	Damping Ratio	Mode Shape							
[]	[Hz]	[]	dof 1	dof 2	dof 3	dof 4	dof 5	dof 6	dof 7	dof 8
1	3.07	0.030	0.32	0.63	0.86	1.00	1.00	0.86	0.62	0.32
2	9.88	0.027	0.88	0.85	-0.08	-1.00	-1.00	-0.08	0.85	0.88
3	27.81	0.024	0.98	-0.35	-0.87	0.64	0.69	-0.86	-0.38	1.00

CHAPTER 5: I-35W BRIDGE DISPLACEMENT ESTIMATION

In this chapter, the dual Kalman filter estimation technique is applied to acceleration data from the southbound structure of the I-35W Saint Anthony Falls Bridge. As discussed in Chapter 4, application of the dual Kalman filter for displacement estimation of an output-only system involves a tuning process. Section 5.1 outlines the tuning process for the I-35W Saint Anthony Falls Bridge system, wherein a range of possible displacements is generated and a 'best guess' at the appropriate tuning parameters is selected. From there, the question of how to track the estimated displacements over time is addressed through the introduction of an event detection method in Section 5.2. The event detection routine is then applied to I-35W Saint Anthony Falls Bridge displacement estimates in Section 5.3, and conclusions are drawn of the validity of the dynamic displacement estimates.

5.1 TUNING THE DKF FOR I-35W BRIDGE DISPLACEMENT ESTIMATION

The acceleration measurements of the October 27, 2010 (night) dynamic truck test 'Open S7' were used to tune the I-35W Saint Anthony Falls Bridge estimation system. 'Open S7' was an open-to-traffic truck test consisting of four waves of two loaded sand trucks traveling in adjacent lanes. French et al. (2012) provides an in-depth description of the dynamic truck tests. The modal parameters used to construct the dynamic model of the I-35W Saint Anthony Falls Bridge for use in the Kalman filter estimation technique were the averages of the hourly system identification results over the period 10/01/2010 – 10/27/2010.

The dual Kalman filter algorithm was run for various combinations of process and input noise covariance parameters to estimate the displacement response from the measured accelerations. Figure 5.1 shows the acceleration error surface over the range of Q^x and Q^p considered for tuning with a measurement noise covariance of $\mathbf{R} = 10^{-7} \times \mathbf{I}$. The measurement noise was approximated from the acceleration measurements of the horizontal accelerometers (ACC 8 and ACC 10). It was assumed that the horizontal accelerations of the bridge are much less than the vertical accelerations and that most of the horizontal acceleration signal was noise. From the acceleration error plot, a region of parameters over which the tuning was assumed to make a difference on the displacement estimates was identified using a similar procedure as that described in Chapter 4.

The range of possible displacement estimate time histories for the region of tuning parameters identified by Figure 5.1 is shown in Figure 5.2 at the location of accelerometer SB SP 2 Ext (midspan of span 2 of the southbound structure) during the dynamic truck test. The displacement estimates shown in the figure are representative of the entire range of displacement estimates. Estimates with significant high frequency content were considered not representative of the physical system. An example of an estimate that was considered to have too much high frequency content is shown with the grey line in Figure 5.2 and was generated by tuning parameters ($Q^x = 10^{-8},\ Q^p = 10^{-17}$). The purple displacement estimate, generated by tuning parameters ($Q^x = 10^{-12},\ Q^p = 10^{-17}$), was selected as the 'best guess' of the true displacements of the I-35W Bridge. These tuning parameters were chosen because they provided displacement estimates that had the largest peak magnitudes while still being

considered smooth. The selection was deemed most representative of the I-35W Bridge response while remaining conservative in the magnitudes of the dynamic displacements.

For the remainder of this report, the tuning parameters from the 'best guess' estimate ($Q^x = 10^{-12}$, $Q^p = 10^{-17}$) are used to model the process noise and input noise for the displacement estimation of the I-35W Saint Anthony Falls Bridge.

5.2 EVENT DETECTION

To quantify and track displacement estimates over time, a systematic procedure was created to identify response events in the displacement estimate time histories. A response event is a portion of the displacement time history that is visibly distinguishable from the baseline displacement estimate, which is considered to be dominated by signal noise. Such a response would likely correspond to the displacements induced from a large vehicle traveling over the bridge. The criteria adopted to define an event are based on the root mean square (RMS) of the displacement record. The existence of an event is determined by the magnitude of the peaks in the RMS record, whereas the duration of the event is defined by locations at which the RMS drops below a certain value. The limits for event detection were set depending on the data under consideration.

The event detection routine is demonstrated on the displacement estimates for the time period in October 2010 during which dynamic truck tests were being conducted (French et al. 2012). The midspan displacement estimate for dynamic truck test 'Open S9' in the early morning of October 28, 2010 is shown in Figure 5.3. 'Open S9' was one wave of eight closely spaced loaded sand trucks travelling at 55 mph $(88\ \mathrm{km/h})$ with the bridge open to traffic. The first, largest peak in the displacement estimate corresponds to the truck test. The other noticeable events are due to normal traffic, possibly cars or trucks. The events (light blue) in the displacement response were systematically identified solely from the RMS record, plotted in the bottom subplot. The RMS calculation is based on a moving window of 2000 points and is smoothed using a 1000-point average. These values were determined experimentally and allowed for easier peak identification of the I-35W Saint Anthony Falls Bridge displacement estimate data. The presence of each event is identified by the peaks larger than 0.002 inches $(0.051\ \mathrm{mm})$ in the RMS record (blue triangle in Figure 5.3 bottom). The duration of the event is defined by a lower cutoff value, set to 0.002 inches as well. When the RMS travels below the cutoff, the event has finished. The first two peaks in the RMS record are within the same event, since the RMS does not drop below the cutoff value between the two peaks. Each response event can be characterized by its largest peak and RMS magnitude over the entire event.

Events are typically easier to systematically identify during low traffic time periods as opposed to high traffic time periods, as there is a lower baseline displacement estimate noise. Due to the varying baseline displacement estimate noise for different traffic conditions, different RMS detection limits for the different times of day must be used to successfully identify events. Figure 5.4 shows the effects of event detection using poor identification limits. If the magnitude RMS limit is not set low enough for a given displacement estimate, certain events may not be identified. Figure 5.4 (left) shows event identification using a magnitude RMS limit of 0.004 inches $0.102\ \mathrm{mm}$), which is clearly too high for this

data set as many events are not identified. If the cutoff frequency to define the length of the event is not set high enough, multiple response events will be grouped into one. Figure 5.4 (right) shows an example of when the set lower cutoff value (0.002 inches) is too low for the data set, and as a result the entire time history is identified as one event. Best results for event identification occurred using time histories during off-peak traffic times (e.g. at night), when larger, distinct events were more likely.

For some displacement estimate records of the I-35W Saint Anthony Falls Bridge, the displacement estimates seem to drift. In the presence of a non-zero mean displacement estimate, the event detection technique based on RMS fails. To handle the drift, displacement estimates can be detrended prior to the event detection routine being implemented. Figure 5.5 shows an example of event detection on a displacement estimate with drift at the end of the time history. The left plot shows the event detection routine implemented on the original estimates, and the right plot shows the event detection routine implemented on the detrended data. Successful identification of the response events is accomplished through detrending.

5.3 EVENT DETECTION ON I-35W BRIDGE DISPLACEMENT ESTIMATES

Displacement estimates were generated for three dates at different times of the I-35W Saint Anthony Falls Bridge's life: October 28, 2010 (dynamic truck tests), July 30, 2013, and January 30, 2014. The modal parameters used to construct the dynamic models were the averages of the hourly system identification results over the period 10/01/2010 – 10/27/2010, 7/10/2013 – 7/30/2013, and 1/10/2014 – 1/30/2014, respectively. These dates were chosen to reflect the possible structural changes due to aging over multiple years (October 28, 2018 & July 30, 2013), as well as to reflect the seasonal variation seen in the natural frequency identification (July 30, 2013 & January 30, 2014). Estimates were generated in the early mornings of the dates given (prior to 7 am), as this allowed for easier identification of the displacement response events.

Table 5.1 shows several parameters describing the displacement estimate event detection results of the three dates considered. For each date, the distribution properties describing the identified events are listed. For example, over all 335 events detected prior to 7 am on October 28, 2010, the largest peak displacement was 0.029 inches $(0.74\ \mathrm{mm})$ and the mean of all 335 peaks in the displacement estimates was 0.011 inches $(0.28\ \mathrm{mm})$. Tracking the properties of the dynamic displacement events over time may serve as an indicator of bridge stiffness; however, as can be seen in Table 5.1 for event data from July 2013 and January 2014, the seasonal variation seen in the natural frequencies (Figure 3.2) is not evident in the displacement estimates. It is unclear if the dynamic displacement data will contain any information regarding bridge stiffness that is not present in the time variation of the natural frequencies themselves.

The resulting maximum displacement estimates are very small (on the order of 0.03 inches). For reference, the dynamic displacement estimates reported for a large suspension bridge that connects Brooklyn with Staten Island were approximately 0.27 inches $(7\ \mathrm{mm})$ when excited by New York City Marathon runners (Kogan et al. 2008). Considering the much longer length (> 4000 ft $(1219\ \mathrm{m})$ main span) and reduced stiffness of the suspension bridge, the dynamic displacement estimates for the I-35W

Saint Anthony Falls Bridge do not seem unreasonable. Comparatively, an October 2010 static truck test with 8 fully loaded trucks generated maximum deflections of 0.8 inches $(20.32\ \mathrm{mm})$, as measured by Olsen Engineering using IBIS-S microwave radar sensor (French et al. 2012). Due to the static deflections being an order of magnitude larger than the estimated peak dynamic displacements, it is possible that the non-zero mean component of the displacement response, which is not captured by the DKF estimation technique, is a large portion of the bridge's total response due to moving loads.

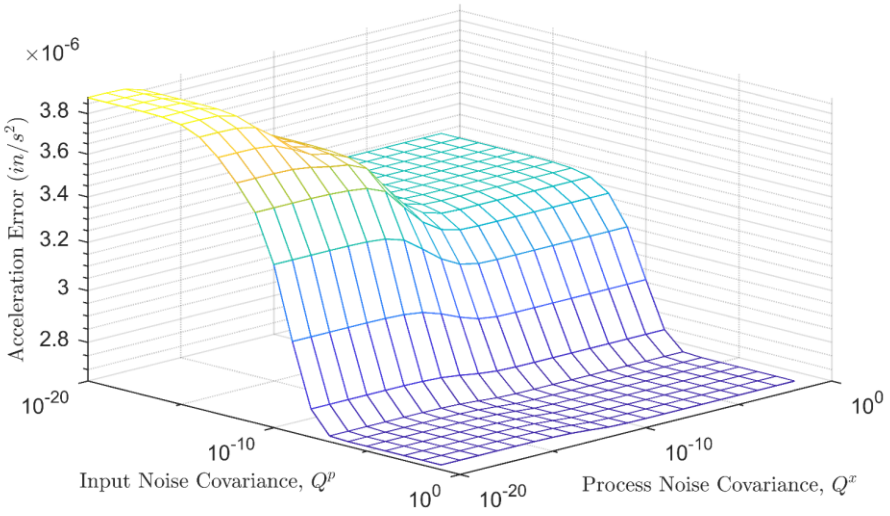

Figure 5.1: Acceleration estimation error surface for I-35W Bridge

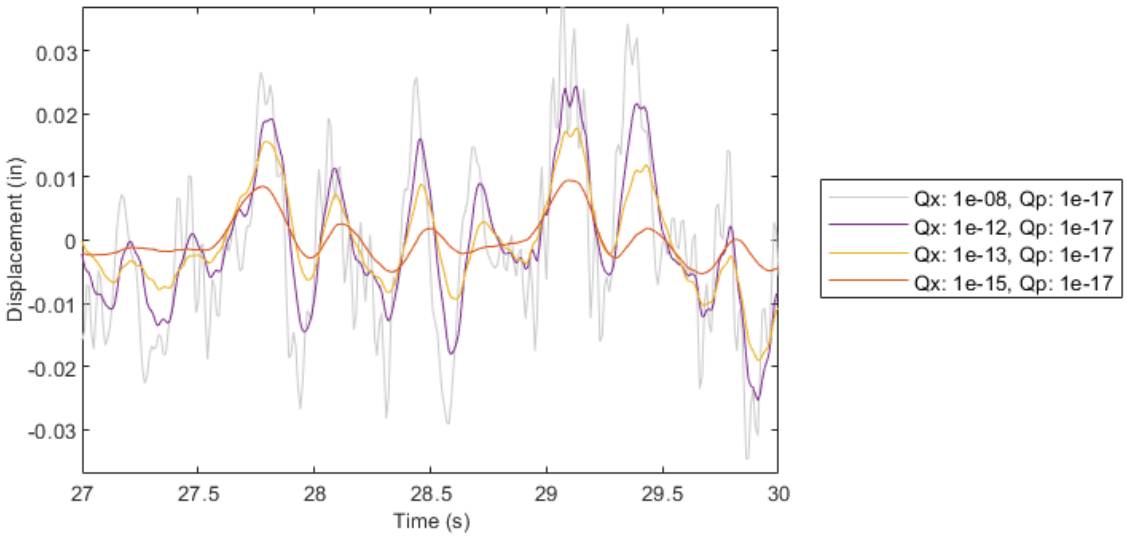

Figure 5.2: Displacement estimate range at SB SP 2 Ext for I-35W Bridge 'Open S7' dynamic truck test

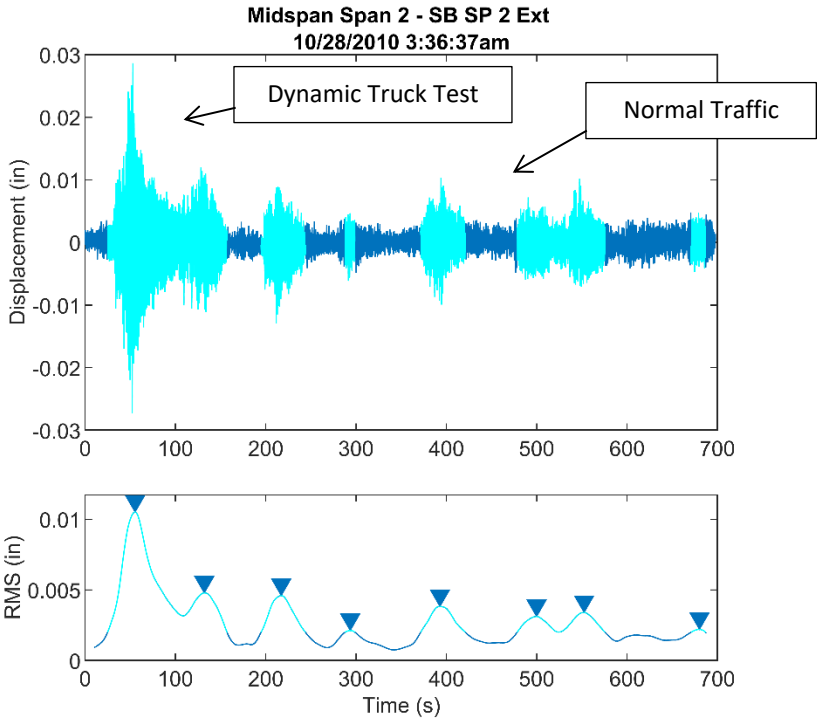

Figure 5.3: 'Open S9' event detection (Top) Displacement estimate with event detection (light blue) and corresponding RMS (Bottom) RMS of displacement estimate, used to identify events

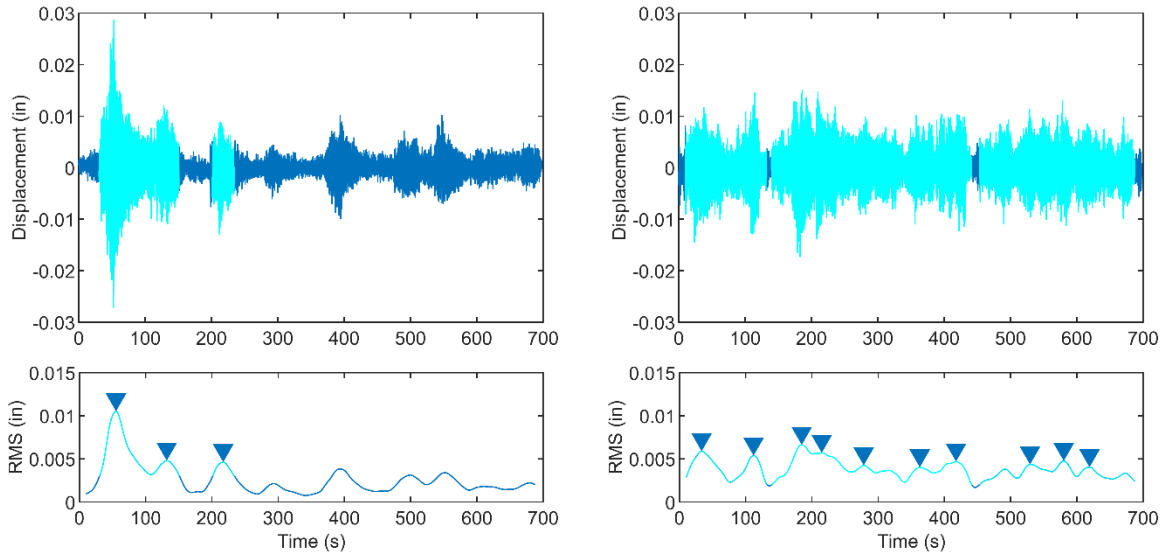

Figure 5.4: Event detection set limits (Left) Event detection with too high RMS peak magnitude limit (Right) Event detection with too low of a cutoff limit

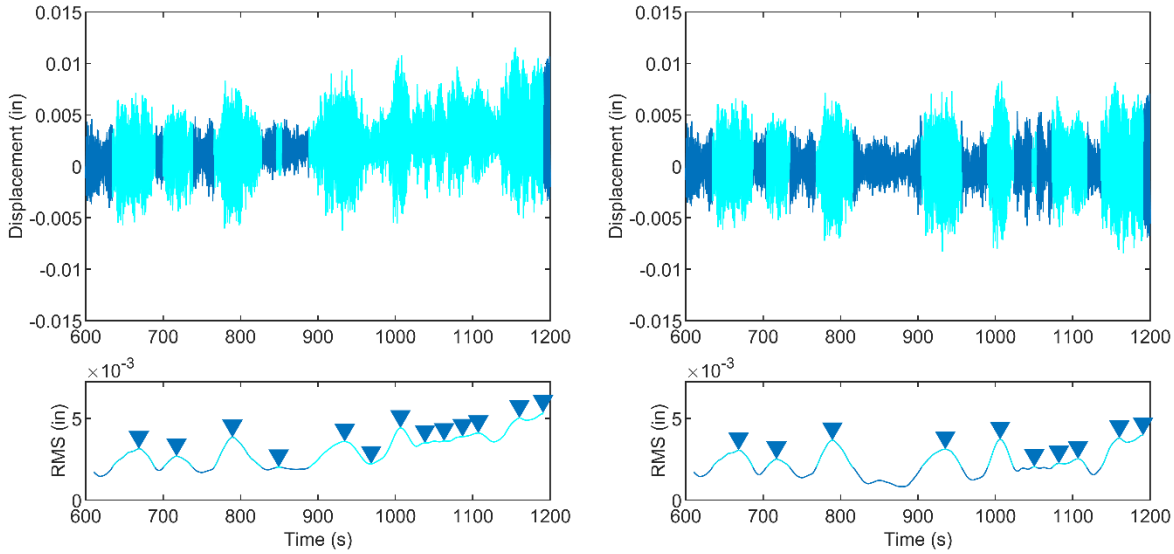

Figure 5.5: Detrending drifted displacement estimate for event detection (Left) Event detection on drifted displacement estimates (Right) Event detection on detrended displacement estimate record

Table 5.1: I-35W Bridge displacement estimation event detection results

Distribution Properties		October 28, 2010**	July 30, 2013	January 30, 2014
Detected Displacement Events	Count	335	94	193
Peak in Displacements (inches)	Max	0.029	0.021	0.033
	Median	0.010	0.007	0.007
	Mean	0.011	0.008	0.008
	Standard Deviation	0.004	0.003	0.003
RMS in Displacements (inches)	Max	0.0080	0.0044	0.0037
	Median	0.0037	0.0023	0.0021
	Mean	0.0040	0.0024	0.0022
	Standard Deviation	0.0010	0.0005	0.0004
Peak in RMS (inches)	Max	0.0128	0.0055	0.0055
	Median	0.0042	0.0022	0.0022
	Mean	0.0048	0.0024	0.0024
	Standard Deviation	0.0019	0.0007	0.0007

* All estimates generated in the early morning of the dates shown (prior to 7 am)
** October 28, 2010 - Dynamic truck test

CHAPTER 6: ESTIMATING MOVING LOADS

The dual Kalman filter (DKF) approach captures only dynamic displacements and not any corresponding static displacement due to relatively slow loading, which may be significant for the moving loads typical on the I-35W Saint Anthony Falls Bridge. To test the hypothesis that non-zero mean displacements are a large portion of the bridge's total response, a SAP2000 model of a concrete girder was built and excited with a moving point load. The model was of one composite girder from Minnesota Department of Transportation Bridge 27568. Properties of the deck and girder are given in Table 6.1. The bridge girder was modeled as a simply supported beam with a transformed section ($\mathrm{I_t} = 416388\ \mathrm{in}^4\ (0.1733\ \mathrm{m}^4), E_\mathrm{c} = 5088\ \mathrm{ksi}\ (35080\ \mathrm{MPa}), w_{sw} = 1868\ \mathrm{lb/ft}\ (27260\ \mathrm{N/m})$). A moving point load was applied to the top of the beam with varying speeds and the elastic dynamic response of the structure was simulated. The magnitude of the moving point load was 50 kips $(222\ \mathrm{kN})$, the approximate total weight of a fully loaded test truck for the October 2010 truck tests (French et al. 2012).

Figure 6.1 shows the maximum displacement response (upward displacement and downward displacement) for the girder with 2% and 10% modal damping for various moving load speeds. A speed of 0 mph corresponds to the static deflection of the girder when loaded at midspan. Overall, the 10% modally damped beam does not displace as much as the 2% modally damped beam. As the speed of the moving load increases, the maximum displacement response increases, up to a certain speed. The speed at which the maximum displacement response is observed roughly corresponds to the first natural frequency of the structure. For a simply supported span, a vehicle traveling across the structure in about the time it takes for the first mode to complete half its cycle will begin to excite that mode. In Figure 6.1, resonance with the first mode is seen for vehicle speeds 65 mph (105 km/h) to 130 mph (209 km/h), which correspond to the half and the full durations of time for the first mode of the Br. 27568 composite girder to complete one cycle. Once the speed of the moving load increases enough to where resonance no longer occurs, then the maximum displacement response decreases and drops below the static loading case. This parallels the displacement transfer function of the beam for different frequency loading.

Perfect tracking of the displacements using the proposed DKF estimation is limited to cases when the structure is resonating or when the moving load is faster than the resonance speed, as these cases cause zero-mean displacements. Figure 6.2 shows the simulated displacement response and the best DKF displacement estimate for the beam midspan when subjected to a 90 mph (145 km/h) moving load. The response looks similar to a free response, and the DKF is able to match the simulated response with great accuracy.

When the speed of the moving load is so slow that it does not excite the first natural frequency, there is a low frequency component of the displacement response that is not captured by the DKF. Figure 6.3 shows the simulated displacement response and the estimated displacement range from the DKF estimation technique at midspan for a moving load traveling at 20 mph (32 km/h). No noise was added to the simulated accelerations for displacement estimation. In Figure 6.3, the time period of the main valley in the displacement response (0-2 seconds) corresponds to when the moving load was acting on

the structure. This low frequency component (main valley) in the displacement response is not captured by the best DKF estimates. Displacement estimates that were able to capture the free response of the structure were not able to capture any of the low frequency part of the displacement response, and estimates that almost captured the low frequency part were poor at matching the free response. The moving load is slow compared to the speed that would be needed to cause resonance with the first mode of the system. Because the DKF is based on a dynamic model of the system, the low frequency portion of the displacement response is not captured by the DKF estimates. When noise is added to the simulated acceleration measurements, the ability of the filter to capture the low frequency component diminishes.

Due to the length and stiffness of the I-35W Saint Anthony Falls Bridge, as well as the complex loading of multiple moving vehicles, it is unlikely that traffic will ever cause resonance with the first mode of the structure. In order for a single vehicle to cause first mode resonance over the main span of the bridge, it would have to travel at several hundred miles per hour. As such, it can be expected that there is a large non-zero mean component of the displacement response when the bridge is excited by traffic that is not captured by the DKF estimation technique.

Originally, GPS was to be used in conjunction with the DKF to estimate the full non-zero mean displacement response. However, the stiffness of the bridge results in low-frequency displacements that are too small to be captured by readily available GPS sensors.

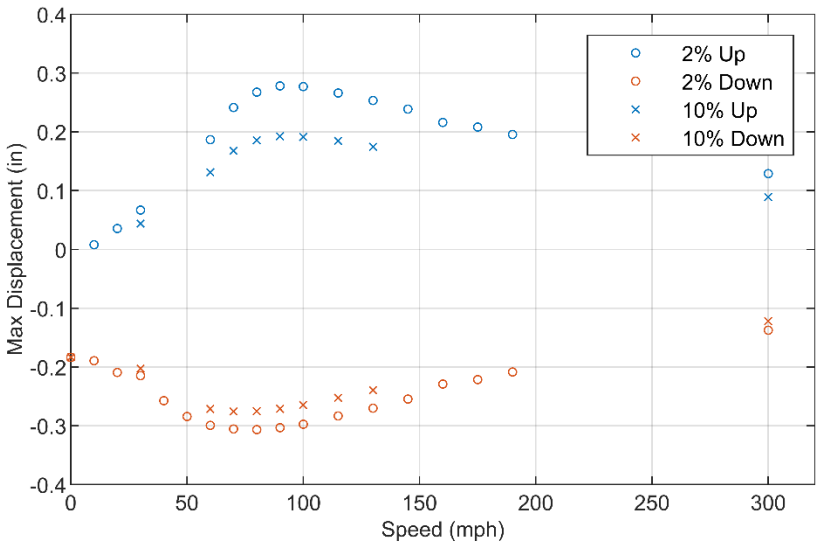

Figure 6.1: Br. 27568 simulated maximum displacement response spectrum

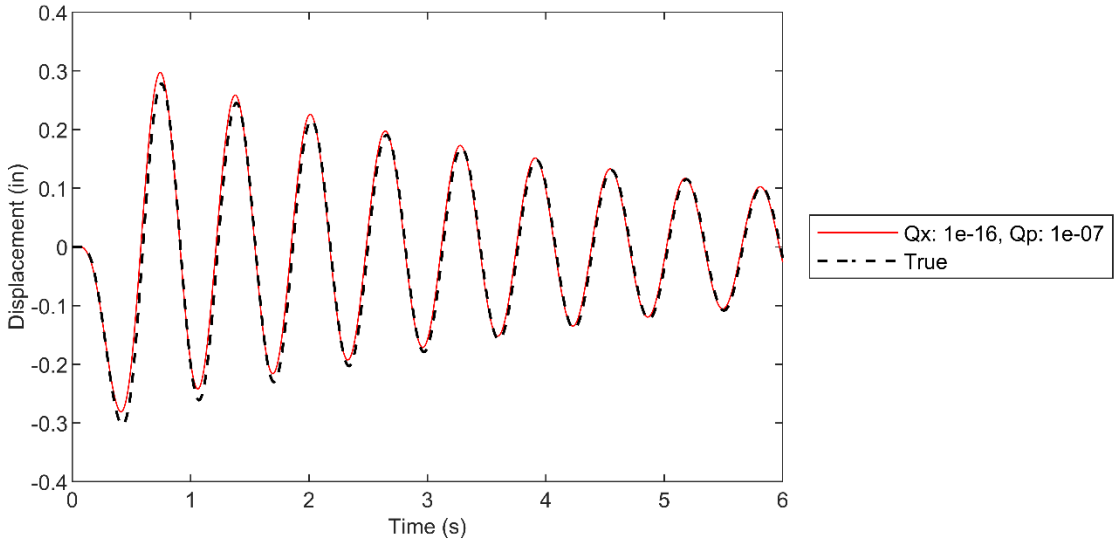

Figure 6.2: Br. 27568 midspan displacement estimate, 90 mph moving load

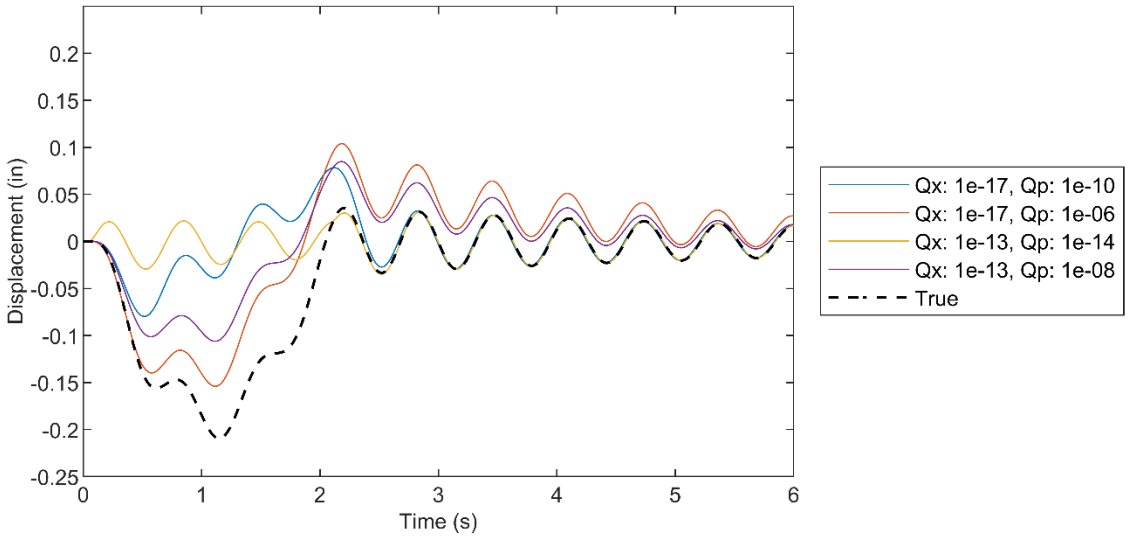

Figure 6.3: Br. 27568 midspan displacement estimate range, 20 mph moving load

Table 6.1: Br. 27568 girder and deck properties

Geometry	Span Length Girder Spacing	60 ft 12 ft o-c
Girder Properties	h_g A_g I_g	45 in 560 in^2 125390 in^4
Girder Concrete Properties	w_{cg} f'_{cg} E_{cg}	150 pcf 7.043 ksi 5088 ksi
Deck Properties	t_d	12 in
Deck Concrete Properties	w_{cg} f'_{cd} E_{cd}	150 pcf 10 ksi 6062 ksi

CHAPTER 7: SUMMARY AND CONCLUSIONS

Given that natural frequency alone was insufficient to determine the health of the I-35W Saint Anthony Falls Bridge, a simpler parameter, vertical displacements, was believed to be better suited to evaluate the performance of the structure. As conventional contact-based displacement measurement methods were not feasible, this study focused on using the currently installed accelerometers to estimate the vertical displacements of the bridge.

The proposed estimation method makes use of dual Kalman filters to estimate both the unknown driving forces to the system (i.e. input) as well as the velocities and displacements (i.e. states). The method is adapted for an output-only application to the I-35W Saint Anthony Falls Bridge, which combines the output-only modal parameters extracted using NExT-ERA/DC in conjunction with the dual Kalman filter (DKF). Even though the input estimates from the DKF hold no physical meaning, it is shown by a simulated example as well as a small-scale laboratory experiment that the DKF outperforms a single Kalman filter under certain excitation conditions.

To achieve accurate estimates of the unobserved input and state, the DKF required a tuning process for proper selection of noise covariance matrices. The process was complicated by measurement noise, but it was shown by a blind case study that conservative displacement estimates can be generated using engineering judgement. The tuning process was applied to the I-35W Saint Anthony Falls Bridge acceleration data, and the parameters for a 'best guess' at the dynamic displacements were selected.

To quantify and track displacement estimates over time, a systematic procedure based on the displacement estimate root mean square was created to identify response events in the displacement estimate time histories. The best results occurred when event identification on displacement estimates was performed at off-peak traffic times due to a lower baseline displacement estimate noise. Tracking the properties of the dynamic displacement events over time could serve as an indicator of bridge stiffness; however, it was unclear if this would contain any information not present in the time variation of the natural frequencies themselves.

Dynamic displacement estimates were generated at different stages of the I-35W Saint Anthony Falls Bridge's life. The seasonal variation seen in the natural frequency was not evident in the displacement estimates and increased displacement magnitudes were not seen over the course of several years. Overall, the peak estimated dynamic displacements, on the order of 0.03 inches, were much smaller than those measured from the static truck tests in October 2010 (0.8 inches).

An analysis of a MnDOT Bridge 27568 girder under a moving load showed that increased deflections should be expected under moving loads, as compared to a static loading. It was found that full displacement response estimation using the proposed dual Kalman filter estimation technique was only successful when the moving load was traveling at or faster than a speed that excites the first natural frequency of the structure. Due to the length and stiffness of the I-35W Saint Anthony Falls Bridge, it can be expected that a large non-zero mean component of the structure's displacement response cannot be captured by the estimation technique.

The non-zero mean component of the displacement response was initially intended to be captured by GPS; however, it was determined that the stiffness of the bridge resulted in low-frequency displacements that were too small to be captured by readily available GPS sensors.

With these considerations in mind, it is recommended that vertical displacement estimation from acceleration measurements using a dual Kalman filter not be implemented further on the I-35W Saint Anthony Falls Bridge. In its present state, the estimation methodology is not appropriate to estimate displacements for such a stiff structure when excited by traffic. However, it is possible that the estimation technique could work well when applied to other structures that are less rigid.

REFERENCES

Azam, S. E., E. Chatzi, and C. Papadimitriou. 2015. “A Dual Kalman Filter Approach for State Estimation via Output-Only Acceleration Measurements.” *Mechanical Systems and Signal Processing* 60: 866–86. doi:10.1016/j.ymssp.2015.02.001.

Franklin, G. F., J. D. Powell, and M. L. Workman. 1998. *Digital Control of Dynamic Systems*. 3rd ed. Menlo Park, CA: Addison-wesley.

French, C. E. W., C. K. Shield, H. K. Stolarski, B. D. Hedegaard, and B. J. Jilk. 2012. “Instrumentation, Monitoring, and Modeling of the I-35W Bridge.” *MN/RC 2012-24*. MnDOT, St. Paul, MN.

Gaebler, K. O. 2017. “Long-Term Vibration Monitoring of the I-35W St. Anthony Falls Bridge.” University of Minnesota, Minneapolis, MN.

Gaebler, K. O., C. K. Shield, and L. E. Linderman. 2017. “Feasibility of Vibration-Based Long-Term Bridge Monitoring Using the I-35W St. Anthony Falls Bridge.” *MN/RC 2017-01*. MnDOT, St. Paul, MN.

Gillijns, S., and B. De Moor. 2007. “Unbiased Minimum-Variance Input and State Estimation for Linear Discrete-Time Systems with Direct Feedthrough.” *Automatica* 43 (5): 934–37. doi:10.1016/j.automatica.2006.11.016.

Gordon, N. J., D. J. Salmond, and A. F. M. Smith. 1993. “Novel Approach to Nonlinear/non-Gaussian Bayesian State Estimation.” *IEE Proceedings F Radar and Signal Processing* 140 (2): 107. doi:10.1049/ip-f-2.1993.0015.

James III, G. H., T. G. Carne, and J. P. Lauffer. 1993. “The Natural Excitation Technique (NExT) for Modal Parameter Extraction From Operating Wind Turbines.” *SAND92-1666*. Sandia National Laboratories, Albuquerque, NM.

Juang, J-N., J. E. Cooper, and J. R. Wright. 1988. “An Eigensystem Realization Algorithm Using Data Correlations (ERA/DC) for Modal Parameter Identification.” *Control Theory and Advanced Technology* 4 (1): 5–14.

Juang, J-N., and R. S. Pappa. 1985. “An Eigensystem Realization Algorithm for Modal Parameter Identification and Model Reduction.” *J. Guidance* 8 (5): 620–27. doi:10.2514/3.20031.

Julier, S. J., and J. K. Uhlmann. 1997. “New Extension of the Kalman Filter to Nonlinear Systems.” *Signal Processing, Sensor Fusion, and Target Recognition VI* (7): 182-94. doi:10.1117/12.280797.

Kalman, R. E. 1960. “A New Approach to Linear Filtering and Prediction Problems.” *Journal of Basic Engineering* 82 (1): 35–45. doi:10.1115/1.3662552.

Kogan, M. G., W-y. Kim, Y. Bock, and A. W. Smyth. 2008. “Load Response on a Large Suspension Bridge during the NYC Marathon Revealed by GPS and Accelerometers.” *Seismological Research Letters* 79 (1): 12–19.

Lee, J. J., and M. Shinozuka. 2006. “A Vision-Based System for Remote Sensing of Bridge Displacement.” *Ndt & E International* 39 (5): 425–31.

Lourens, E., C. Papadimitriou, S. Gillijns, E. Reynders, G. De Roeck, and G. Lombaert. 2012. “Joint Input-Response Estimation for Structural Systems Based on Reduced-Order Models and Vibration Data from a Limited Number of Sensors.” *Mechanical Systems and Signal Processing* 29: 310–27. doi:10.1016/j.ymssp.2012.01.011.

Lourens, E., E. Reynders, G. De Roeck, G. Degrande, and G. Lombaert. 2012. “An Augmented Kalman Filter for Force Identification in Structural Dynamics.” *Mechanical Systems and Signal Processing* 27 (1): 446–60. doi:10.1016/j.ymssp.2011.09.025.

Maes, K., E. Lourens, K. Van Nimmen, E. Reynders, G. De Roeck, and G. Lombaert. 2015. “Design of Sensor Networks for Instantaneous Inversion of Modally Reduced Order Models in Structural Dynamics.” *Mechanical Systems and Signal Processing*. doi:10.1016/j.ymssp.2014.07.018.

Nassif, H. H., M. Gindy, and J. Davis. 2005. “Comparison of Laser Doppler Vibrometer with Contact Sensors for Monitoring Bridge Deflection and Vibration.” *Ndt & E International* 38 (3): 213–18. doi: 10.1111/j.1747-1567.2006.00132.x.

Nayeri, R. D., F. Tasbihgoo, M. Wahbeh, J. P. Caffrey, S. F. Masri, J. P. Conte, and A. Elgamal. 2009. “Study of Time-Domain Techniques for Modal Parameter Identification of a Long Suspension Bridge with Dense Sensor Arrays.” *Journal of Engineering Mechanics* 135 (7): 669–83. doi:10.1061/(ASCE)0733-9399(2009)135:7(669).

Pappa, R. S., K. B. Elliott, and A. Schenk. 1993. “Consistent-Mode Indicator for the Eigensystem Realization Algorithm.” *Journal of Guidance, Control, and Dynamics* 16 (5): 852–58. doi:10.2514/3.21092.

Park, J. W., S. H. Sim, and H. J. Jung. 2013. “Displacement Estimation Using Multimetric Data Fusion.” *IEEE/ASME Transactions on Mechatronics* 18 (6): 1675–82. doi:10.1109/TMECH.2013.2275187.

Petersen, W., O. Øiseth, T. S. Nord, and E. Lourens. 2018. “Estimation of the Full-Field Dynamic Response of a Floating Bridge Using Kalman-Type Filtering Algorithms.” *Mechanical Systems and Signal Processing* 107: 12–28. doi:10.1016/j.ymssp.2018.01.022.

Tatsis, K., and E. Lourens. 2016. “A Comparison of Two Kalman-Type Filters for Robust Extrapolation of Offshore Wind Turbine Support Structure Response.” In *Life-Cycle of Engineering Systems: Emphasis on Sustainable Civil Infrastructure: Proceedings of the Fifth International Symposium on Life-Cycle Civil Engineering (IALCCE 2016)*, 209. Delft, The Netherlands: CRC Press.

Xia, Y., H. Hao, G. Zanardo, and A. Deeks. 2006. “Long Term Vibration Monitoring of an RC Slab: Temperature and Humidity Effect.” *Engineering Structures* 28: 441–52. doi:10.1016/j.engstruct.2005.09.001.

APPENDIX A
MONITORING SYSTEM OUTAGES

This Appendix contains a list of I-35W Saint Anthony Falls Bridge monitoring system operation and maintenance issues as well as the steps taken to address those issues. This list is in no way complete but is intended to serve as an additional reference for future troubleshooting scenarios and data analysis.

Approximate periods of data loss are given for each subsystem in Table A1. If available, detailed information on each outage is provided. Undocumented outages in the data files are reported for periods lasting longer than one day. All static system outages have been documented. Missing dynamic system data with undocumented causes are reported over the period 4/1/2010 – 6/30/2018. SOFO data missing from "C:\UMN Data Monitoring\SOFO2.csv" with undocumented causes are reported over the period 10/27/2010 – 6/8/2018.

Table A1: Monitoring system data outages

Subsystem	Missing Data	Portion Effected	Cause
Static System	11/8/2010 – 12/15/2010	SB datalogger	A/D Power Converter Malfunction
	8/6/2016 – 10/18/2016	NB datalogger	Bad Battery
	10/2/2017 – 1/17/2018	SB datalogger	Faulty Media Converter
Dynamic System	8/15/2009 – 9/28/2009	Nodes 1-8	Lightning
	Winter 2009 – 2010	Node 8 LPs	LP Braces Contacting Vermin Guard
	5/22/2010 – 5/26/2010	Nodes 1-8	Undocumented
	6/25/2010 – 9/19/2010	Nodes 1-8	Lightning
	10/11/2010	Nodes 1-8	Undocumented
	11/12/2010	Node 5	Undocumented
	5/1/2011	Node 5	Undocumented
	6/25/2011 – 9/13/2011	Nodes 1-8	Poor Synchronization Signal
	12/29/2011	Node 8	Undocumented
	5/19/2012	Nodes 3-8	Undocumented
	5/27/2012 – 2/5/2013	Nodes 1-8	Lightning
	2/15/2013	Nodes 7-8	Undocumented
	6/21/2013 – 8/6/2013	Nodes 4-8	Lightning
	9/5/2013	Nodes 1-8	Undocumented
	9/20/2013 – 9/23/2013	Nodes 1-8	Undocumented
	4/27/2014 – 7/11/2014	Nodes 4-8	Communication Loss
	8/21/2014 – 8/28/2014	Nodes 4-8	Lightning
	9/20/2014 – 2/9/2015	Nodes 4-8	Lightning
	1/19/2015 – 1/21/2015	Nodes 1-3	Server Issues
	6/20/2015 – 6/22/2015	Nodes 4-8	Lightning
	7/6/2015 – 7/20/2015	Nodes 4-8	Lightning
	8/7/2015 – 8/18/2015	Nodes 4-8	Communication Loss
	9/6/2015 – 9/9/2015	Nodes 4-8	Lightning
	12/20/2015 – 1/6/2016	Nodes 1-8	Server Issues
	9/6/2016 – 9/8/2016	Nodes 4-8	Communication Loss
	9/21/2016 – 9/22/2016	Nodes 3-8	Communication Loss
	11/29/2016	Nodes 1-8	Undocumented
	10/2/2017 – 1/20/2018	Nodes 4-8	Lightning
	5/28/2018 – 5/30/2018	Nodes 1-8	Lightning

SOFO System	10/27/2010 – 10/29/2010	All gages	Software, Firmware Out of Date
	2/24/2011 – 3/2/2011	All gages	Undocumented
	5/18/2011 – 5/23/2011	All gages	Undocumented
	2/7/2012 – 2/22/2012	All gages	Database File Size Limit
	6/7/2012 – 6/8/2012	All gages	Undocumented
	8/23/2012 – 8/27/2012	All gages	Undocumented
	11/23/2012 – 11/25/2012	All gages	Undocumented
	1/8/2013 – 1/13/2013	All gages	Undocumented
	9/14/2013 – 9/15/2013	All gages	Undocumented
	10/14/2013 – 11/1/2013	All gages	Undocumented
	2/1/2014 – 2/3/2014	All gages	Undocumented
	8/27/2014 – 8/28/2014	All gages	Undocumented
	9/10/2014 – 9/23/2014	All gages	Presumed Connectivity Issue
	5/11/2015 – 5/27/2015	All gages	Presumed Connectivity Issue
	7/25/2015 – 7/30/2015	All gages	Undocumented
	9/22/2015 – 10/21/2015	All gages	Undocumented
	1/4/2016 – 1/5/2016	All gages	Undocumented
	4/15/2016 – 4/29/2016	All gages	Database File Size Limit
	9/1/2016 – 9/6/2016	All gages	Undocumented
	1/6/2017 – 1/9/2017	All gages	Undocumented
	4/28/2017 – 5/1/2017	All gages	Undocumented
	9/17/2017 – 9/22/2017	All gages	Database File Size Limit
Corrosion Monitoring System	Bridge Opening – present	All gages	Data Not Understood

Corrosion Monitoring System Difficulties: Bridge Opening – present

The CorSenSys corrosion monitoring system has never been fully operational since the system was installed. No user's manual has been provided by the suppliers, and the collected data has never been fully analyzed or understood. Prior to April 14, 2011 none of the dataloggers provided data usable for any sort of monitoring. On April 14, 2011, two of the dataloggers were replaced (503 was replaced by 402, and 504 was replaced by 401). These dataloggers appear to provide data that might be usable for monitoring, but because no user's manual has been provided, interpretation of the data has proven impossible. The two remaining dataloggers were replaced on September 13, 2011 (505 was replaced by 403, 506 was replaced by 404). Again, the new dataloggers appear to provide data that might be usable, but without a user's manual interpretation has been impossible.

Linear Potentiometer Outage: Bridge Opening – 9/28/2009

The four LPs attached to the southbound bridge at Pier 4 were not collecting data at bridge opening. It was found that the LPs were operational but were not powered properly. This issue was resolved on September 28, 2009, and approximately one full year of data was lost since bridge opening.

LP Data Loss:

SB SP3 Ext:	bridge opening – 9/28/2009
SB SP3 Int:	bridge opening – 9/28/2009
SB SP4 Ext:	bridge opening – 9/28/2009
SB SP4 Int:	bridge opening – 9/28/2009

SOFO System Problems: 10/30/2008 – 1/9/2010

From October 30, 2008 until January 9, 2010, the data collection from the static system was often erratic. The system would randomly miss data readings. Although the system was scheduled to read every hour, it would occasionally skip sensors. Occasionally, these skips would be chronic, and one sensor would appear to be down for several days at a time, and these chronic problems were not necessarily unique to any particular sensor. When the system did manage to read the sensors, the strain values appeared to be reasonable. This issue was resolved by Smartec (the system supplier) on January 9, 2010 with an update to the data collection software and data-logger firmware.

SOFO Data Loss (Erratic):

Various gages:	10/30/2008 – 1/9/2010

Dynamic System Outage: 8/15/2009 – 9/28/2009

The entire dynamic system was shut down on August 15, 2008. The timing for the outage appeared to coincide with electrical storms in the area. System repairs involved replacement of the data-logger boards or repeater nodes (which connect data-logger nodes together).

Accelerometer and LP Data Loss:

Nodes 1-8:	8/15/2009 – 9/28/2009

Linear Potentiometer Erroneous Readings: Winter 2009-2010

It was discovered that the LP braces extending down to the top of Pier 3 from the interior box of southbound bridge Span 3 were colliding with the vermin guard across the expansion joint. This caused erroneous LP readings during the winter of 2009-2010. On June 18, 2010, the vermin guard was sufficiently trimmed back for all LP braces extending down to Pier 3.

Dynamic System Outage: 6/25/2010 – 9/19/2010

The entire dynamic system was shut down on June 25, 2010. The timing for the outage appeared to coincide with electrical storms in the area. Approximately half of the system (Nodes 1 through 5) was brought online on August 28, 2010. Nodes 6, 7, and 8 were brought online on September 19, 2010. System repairs involved replacement of the data-logger boards or repeater nodes.

It was found that four of the linear potentiometers had failed during the outage. The two LPs attached to the northbound bridge at Abutment 1 were replaced September 21, 2010, and the two LPs attached to Span 4 of the southbound bridge at Pier 4 were replaced September 30, 2010. For these replacements, the new LPs were mounted on the same concrete embedded bolts as were used to mount the replaced LPs.

Accelerometer and LP Data Loss:

Nodes 1-5*:	6/25/2010 – 8/28/2010
* NB SP1 Ext (LP):	6/25/2010 – 9/21/2010
* NB SP1 Int (LP):	6/25/2010 – 9/21/2010
* SB SP4 Ext (LP):	6/25/2010 – 9/30/2010
* SB SP4 Int (LP):	6/25/2010 – 9/30/2010
Nodes 6-8:	6/25/2010 – 9/19/2010

Static System Outage: 11/8/2010 – 12/15/2010

On October 28, 2010, the power supply that converted AC power to 12V DC for the fiber optic converters inside the control shed failed. This failure cut off connection between the server and dataloggers located inside the bridge. The dataloggers continued to run and collect data without continuous connection to the server. The power-supply was replaced on January 4, 2011. It was found that the northbound bridge datalogger did not lose any data; the onboard hard disk had enough storage space such that none of the data collected during the outage was overwritten. The datalogger in the southbound bridge, which collected data from more sensors but had the same size of hard disk as the northbound datalogger, overwrote data from November 8, 2010 to December 15, 2010. This data was not recoverable.

Vibrating Wire Strain Gage and Thermistor Data Loss:

Northbound Structure:	no data loss
Southbound Structure:	11/8/2010 – 12/15/2010

Dynamic System Outage: 6/25/2011 – 9/13/2011

On June 25, 2011, difficulties were encountered when attempting to collect data from Nodes 5-8 simultaneously with Nodes 1-4. Collecting Nodes 5-8 without Nodes 1-4 worked, as did collecting Nodes 1-4 without 5-8, but collecting both sets at the same time was not possible. The problem was discovered to be a poor synchronization signal between Nodes 4 and 5. On September 13, 2011, Node 5 was replaced and the issue was resolved.

Accelerometer and LP Data Loss:

Nodes 1-4:	6/25/2011, 7/6/2011 – 7/21/2011, 8/10/2011 – 8/11/2011
Nodes 5-8:	6/25/2011- 8/9/2011, 8/12/2011 – 9/13/2011

Comments:

1. During the repairs performed on September 13, 2011, an additional wire was tied from a point near the accelerometer channels of Node 5 to ground. Josh Sebasky from Minnesota Measurements stated that this was to "augment" the ground. It was noted that Ken Spikowski from Dataq found manifestations of a weak ground in the Node 5 accelerometer data (the accelerometers would occasionally and temporarily lose their 1g stable point). Josh Sebasky mentioned that the grounds used for all the Dataq nodes were tied into the lighting system, for which the electrical work was supplied by Polyphase. He believed that the ground had been weak for Node 5 ever since installation, but it would not be possible to rectify this situation short of tying to a new ground outside the lighting system. It was not clear if the weak ground at Node 5, or the grounding scheme in general, had any implications regarding the cause of the aforementioned failures, nor was it clear whether the annual summer system failures would continue in the future.

SOFO System Outage: 2/7/2012 – 2/22/2012

On February 7, 2017, an error caused no data to be collected from the SOFO sensors. A dialog box appeared that stated: *"Run-time error '3219': Operation is not allowed in this context''.* The system supplier (Smartec) was contacted and a representative created a new database file from the old one that was starting to become too large. On February 22, 2012, the new database file was online and the system began collecting data as usual.

Comments:

1. The old database file was saved as "South_Bound_exterior_Copy_2012_02_22.sdb". Some of the data on this file has never been processed to compute average hourly strains. As a result, the "C:\UMN Data Monitoring\SOFO2.csv" comma-delimited file that contains average hourly strains has data missing from 10/8/2011 to 2/22/2012.

SOFO Data Loss:

All gages:	2/7/2012 – 2/22/2012

Dynamic System Outage: 5/27/2012 – 2/5/2013

The entire dynamic system was shut down on May 7, 2012. The timing for the outage appeared to coincide with electrical storms in the area. System repairs involved replacement of the data-logger boards or repeater nodes (which connect data-logger nodes together) on January 9, 2013. Eight of the linear potentiometers were not collecting data after the system was brought back online, including NB SP1 Int, NB SP1 Ext, NB SP4 Int, SB SP 1 Ext, SB SP1 Int, SB SP3 Ext, SB SP3 Int, and SB SP4 Int. Each of these was replaced on February 5, 2013.

It was discovered that some of the multiplexer channels to which the LPs were originally connected were no longer functioning. Therefore, the LPs connected to Nodes 1, 3, and 4 were moved to new channels. The channel swap required that the Node 1 LPs be moved from collection channels 1 through 4 to channels 3 through 6. All other LPs kept the same collection channels as before. In the process of changing channels, the data from Node 4 (Southbound Span 1) were significantly altered; the data jumped substantially with respect to the previous readings on May 27, 2012. Because no evidence of substantial bridge movement was seen in any other data, it was believed that this jump was nonphysical. Channel switches on Nodes 1 and 3 did not appear to cause any notable jumps. On April 8, 2013 the LP connection at Node 4 were moved which mostly reversed the jump in readings. Following this channel swap, LP readings from Node 4 were only approximately 0.2 in. (5 mm) off from expected values from the previous year. Therefore, it was concluded that this jump in data was caused by damaged signal board channels. The channel swaps performed due to this outage are outlined in detail in (French et. al., 2014)

Accelerometer and LP Data Loss:

Node 1-2*:	5/27/2012 – 8/23/2012
* NB SP4 Int (LP):	5/27/2012 – 2/5/2013
Nodes 3-8*:	5/27/2012 – 1/9/2013
* NB SP1 Int (LP):	5/27/2012 – 2/5/2013
* NB SP1 Ext (LP):	5/27/2012 – 2/5/2013
* SB SP1 Int (LP):	5/27/2012 – 2/5/2013
* SB SP1 Ext (LP):	5/27/2012 – 2/5/2013
* SB SP3 Int (LP):	5/27/2012 – 2/5/2013
* SB SP3 Ext (LP):	5/27/2012 – 2/5/2013
* SB SP4 Int (LP):	5/27/2012 – 2/5/2013

Dynamic System Outage: 6/21/2013 – 8/6/2013

Following a lightning storm on June 21, 2013, only Nodes 1, 2, and 3 continued to collect. The remainder of the nodes were brought back online on July 8, 2013 without the replacement of any nodes. However, it was later discovered that while the Node 4 board was still operating, the data from that node was corrupt, thus indicating the need for replacement. Node 4 was replaced on August 6, 2013, resolving the issue. It was found that the linear potentiometer at Southbound Span 1 interior box was damaged; the sensor was replaced on July 25, 2013.

Accelerometer and LP Data Loss:

Nodes 1-3:	minimal data loss
Node 4*:	6/21/2013 – 8/6/2013
* SB SP1 Int (LP):	6/21/2013 – 7/25/2013
Nodes 5-8:	6/21/2013 – 7/8/2013

Dynamic System Outage: 4/27/2014 – 7/11/2014

Communication to Nodes 4 through 8 was lost on April 27, 2014, though Nodes 1, 2, and 3 still continued to collect data. On July 11, 2014, DI-720 boards were replaced at Node 3 and Node 6. Full communication to all eight nodes was regained. Upon regaining communication, Node 7 accelerometer readings were way out-of-bounds. Also, the LPs attached to Node 4 (southbound bridge Span 1) provided no signal.

Accelerometer and LP Data Loss:

Nodes 1-3:	minimal data loss
Nodes 4-8:	4/27/2014 – 7/11/2014

Dynamic System Outage: 8/21/2014 – 8/28/2014

On August 21, 2014, a presumed lightning strike silenced Nodes 4-8 of the dynamic system. Power was cycled at Node 4 on August 28, 2014 and the system was brought back online.

Accelerometer and LP Data Loss:

Nodes 1-3:	minimal data loss
Node 4-8:	8/21/2014 – 8/28/2014

SOFO System Outage: 9/10/2014 – 9/23/2014

The weekly email on September 15, 2014 pointed out that the SOFO Fiber Optic system was not responding. It was believed to be a connectivity issue. Repairs to bring the system back online included (1) making sure the COM cable was properly connected to the SOFO and (2) restarting the SOFO data logger (turn off and on the power button). Paul Reichstadt was able to get the system working on September 23, 2014.

SOFO Data Loss:

All gages:	9/10/2014 – 9/23/2014

Dynamic System Outage: 9/20/2014 – 2/9/2015

On September 20, 2014, electrical storms in the area caused Nodes 5-8 to stop communicating. Nodes 1-3 restarted recording automatically, but Nodes 4-8 could no longer be accessed. The September 20, 2014 files showed no sensor problems. On February 9, 2015, power was cycled on Node 4 and restored connection to the southbound nodes.

Accelerometer and LP Data Loss:

Nodes 1-3:	minimal data loss
Nodes 4-8:	9/20/2014 – 2/9/2015

Server Issues: 1/19/2015 – 1/21/2015

On January 19, Ken Spikowski (Dataq) noticed that the server was bogged down and was causing data acquisition problems. Paul Reichstadt was able to restart the server on January 21, 2015.

Accelerometer and LP Data Loss:

Nodes 1-3:	1/19/2015 – 1/21/2015

SOFO System Outage: 5/11/2015 – 5/27/2015

Weekly emails in pointed out that the SOFO Fiber Optic system was not responding. It was believed to be a connectivity issue, and repairs to bring the system back online included (1) making sure the COM cable was properly connected to the SOFO and (2) restarting the SOFO data logger (turn off and on the power button). The system was brought back online May 27, 2015.

SOFO Data Loss:

All gages:	5/11/2015 – 5/27/2015

Dynamic System Outage: 6/20/2015 – 6/22/2015

A presumed lightning strike caused dynamic system Nodes 4-8 to stop communicating on June 20, 2015. Cycling power on Node 4 (from inside the bridge) on June 22, 2015 allowed communications to be regained to all nodes.

Accelerometer and LP Data Loss:

Nodes 1-3:	minimal data loss
Nodes 4-8:	6/20/2015 – 6/22/2015

Dynamic System Outage: 7/6/2015 – 7/20/2015

A presumed lightning strike caused dynamic system Nodes 4-8 to stop communicating on June 20, 2015. On July 20, 2015, all nodes were found spontaneously to be responding. No other sensor problems were found.

Accelerometer and LP Data Loss:

Nodes 1-3:	minimal data loss
Nodes 4-8:	7/6/2015 – 7/20/2015

Dynamic System Outage: 8/7/2015 – 8/18/2015

In the morning of August 7, 2015, the southbound nodes (Nodes 4-8) quit communicating during the 5 minutes when acquisition was stopped during changeover of daily files. Power cycling Node 4 on August 18, 2015 allowed communication to be regained to all nodes.

Accelerometer and LP Data Loss:

Nodes 1-3:	minimal data loss
Nodes 4-8:	8/7/2015 – 8/18/2015

Dynamic System Outage: 9/6/2015 – 9/9/2015

A presumed lightning strike caused dynamic system Nodes 4-8 to stop communicating on September 6, 2015. On September 9, 2015, cycling power to Node 4 allowed communication to be regained to all nodes.

Accelerometer and LP Data Loss:

Nodes 1-3:	minimal data loss
Nodes 4-8:	9/6/2015 – 9/9/2015

Server Issues: 1/5/2016

Around January 5, 2016 the server crashed. Some of the dynamic system daily data files leading up to and immediately following the crash are of unusually short duration.

Unusual Accelerometer and LP Data Files:

All Nodes:	12/20/2015, 12/29/2015, 12/30/2015, 1/4/2016, 1/5/2016, 1/6/2016

SOFO System Outage: 4/15/2016 – 4/29/2016

The SOFO reading unit entered a continual reset mode upon launch for a week at the end of April 2016, due to the database file becoming too large. Paul Reichstadt was able to reset the SOFO unit.

SOFO Data Loss:

All gages:	4/15/2016 – 4/29/2016

Static System Outage: 8/6/2016 – 10/18/2016

Data was not collected from the northbound static system data logger starting August 6, 2016 because of a bad battery. The northbound data logger battery was replaced with a temporary battery on September 22, 2016. Data collection was restarted on October 18, 2016. The northbound and southbound static data logger batteries were replaced with new batteries on April 28, 2017.

Vibrating Wire Strain Gage and Thermistor Data Loss:

Northbound Structure: 8/6/2016 – 10/18/2016
Southbound Structure: no data loss

Comments:

1. Weekly emails now include static data logger battery voltages, which are taken from the most recent recordings in the static data files. Therefore, battery voltages reported in the emails will not be current if data files are not current (i.e. due to connectivity issues that cause data loss, etc.).

Dynamic System Outage: 9/6/2016 – 9/8/2016

Nodes 4, 5, 6, 7, and 8 of the dynamic data collection system were not operational on September 6, 2016. As a result, the accelerometers and linear potentiometer data was not collected from the south bound structure. On September 8, 2016, power was cycled at Node 4 (someone had to enter the bridge and cycle power manually) and the system was operational again.

Accelerometer and LP Data Loss:

Nodes 1-3: minimal data loss
Nodes 4-8: 9/6/2016 – 9/8/2016

Dynamic System Outage: 9/21/2016 – 9/22/2016

Nodes 3, 4, 5, 6, 7, and 8 of the data collection system were not operational on September 21, 2016. As a result, the accelerometers and linear potentiometer data was not collected from the southbound structure. On September 22, 2016, power was cycled for the entire structure and the nodes became operational again. Power cycling was achieved at ground level in an electrical box on the east side of the I-35W Northbound off ramp at University Avenue. Contact Paul Reichstadt for more information.

Accelerometer and LP Data Loss:

Nodes 1-2: minimal data loss
Nodes 3-8: 9/21/2016 – 9/22/2016

SOFO System Outage: x 9/17/2017 – 9/22/2017

On September 17, 2017, an error caused no data to be collected from the SOFO sensors. The following error message was given in a pop-up window: *"Run-time error '-2147217887 (80040e21)': Cannot open database ''. It may not be a database that your application recognizes, or the file may be corrupt."* This error occurs when the SOFO database becomes too large and no more data can be added to the file. There is an automatic file backup that should prevent the error, but for some reason it had not been occurring. On September 22, 2017, the file was manually backed up by going to the "C:\Data\Smartec" directory and running the CloneSDB.bat executable, and normal data collection operation was restored.

SOFO Data Loss:

All gages: 9/17/2017 – 9/22/2017

Dynamic System Outage: 10/2/2017 – 1/20/2018

A dynamic system error was detected on October 2, 2017. The timing for the outage appeared to coincide with electrical storms in the area. The southbound Dataq collection Nodes 4, 5, 6, 7, and 8 would not respond to a communication PING. Power cycling did not fix the issue. Electrical circuit boards (DI-720 A/D board) were replaced at Nodes 3, 4, 5, and 6 by October 31, 2017 and solved communication issues to all nodes. An Ethernet surge suppressor was replaced at Node 4. The following table lists the configurations of the hardware now installed:

Node	IP Address	MAC Address	Serial #
1	192.168.0.131	00:90:C2:DF:E2:7B	484D43DF
2	192.168.0.129	00:90:C2:E0:06:02	4C6D9A80
3	192.168.0.130	00:90:C2:E7:74:BA	50491C33
4	192.168.0.127	00:90:C2:D9:98:FD	4C6DA2A2
5	192.168.0.133	00:90:C2:DC:6E:DA	4AC23375
6	192.168.0.134	00:90:C2:E9:D7:45	4A8C6875
7	192.167.0.128	00:90:C2:CB:58:5A	4849A249
8	192.168.0.135	00:90:C2:E7:FB:27	4C5ADB8A

The linear potentiometer (LP) located in the exterior box of the southbound structure measuring motion relative to the south abutment (SB SP1 EXT) also began malfunctioning on October 2, 2017. It was sent to the manufacturer (UniMeasure) for repairs and re-installed in the bridge on January 18, 2018. Upon installation of the refurbished LP, it was detected that the channel in the filter board of Node 4 was malfunctioning. The SB SP1 EXT linear potentiometer was changed from filter board screw terminal 37 to screw terminal 34. This decision reordered the two LPs at Node 4 in the raw live collection file (NODE4.wdh). The change was reflected in the Dataq system with a proper name change and was addressed in the daily file (NODE4.WDH) to match the channel order from before the outage. No other changes to data monitoring software were necessary as all UMN data monitoring programs reference the daily file.

Accelerometer and LP Data Loss:

Nodes 1-3:	no data loss
Nodes 4-5*:	10/2/2017 – 10/12/2017
* SB SP1 EXT (LP):	10/2/2017 – 1/20/2018
Nodes 6-8:	10/2/2017 – 10/30/2017

Comments:

1. Two spare electrical circuit boards configured for Dataq Nodes are currently stored at the University of Minnesota (UMN). They are property of the Minnesota Department of Transportation. Configuration of the hardware stored at UMN:

Node	IP Address	MAC Address	Serial #
3	192.168.0.133	00:90:C2:E0:56:F2	4C59D834
4	192.168.0.134	00:90:C2:E9:D9:54	4AC3D2D0

Static System Outage: 10/2/2017 – 1/17/2018

Email warnings stated that no new data from the static system was being collected from the southbound data logger. After inspection, it was determined that the outage occurred on October 2, 2017 due to a communication issue between the server and southbound data logger caused by a faulty fiber optic to Ethernet media converter located in the bridge. The conclusion that the media converter was at fault was a difficult one to come to, as communications from the server shed through the faulty converter to a laptop could be achieved but the server could not PING the data logger through the converter. A laptop could directly connect to the data logger and it could be seen that the logger was functioning properly, therefore the media converter was presumed to be malfunctioning. The faulty converter was replaced on February 6, 2018 and communication to the southbound data logger was regained. The southbound bridge datalogger overwrote data from October 2, 2010 to January 17, 2010. This data was not recoverable.

Vibrating Wire Strain Gage and Thermistor Data Loss:

Northbound Structure: no data loss

Southbound Structure: 10/2/2017 – 1/17/2018

Comments:

1. The southbound data logger can store approximately two weeks worth of data before being overwritten.

Dynamic System Outage: 5/28/2018 – 5/30/2018

Ken Spikowski (Dataq) noticed that the dynamic system went down May 28, 2018. The timing for the outage appeared to coincide with electrical storms in the area. Power cycling the dynamic system at the breaker box caused all of the nodes to come back online on May 28, 2018.

Accelerometer and LP Data Loss:

Nodes 1-8: 5/28/2018 – 5/30/2018

APPENDIX B
THE DUAL KALMAN FILTER

The dual implementation of the Kalman filter for the unknown state and input estimation via output-only acceleration measurements was first introduced by Azam et al. (2015). State estimation of a partially observed dynamic system in a stochastic framework has been studied extensively, and many algorithms have been developed for linear and nonlinear state-space models. When applied to structural dynamics problems, a majority of the methods (e.g., Kalman 1960; Julier and Uhlmann 1997; Gordon, Salmond, and Smith 1993) assume knowledge of the driving forces to the system, some output measurements, and a model of the system.

In practice, it is generally not possible to measure the input to the system or accurately predict the driving forces. A common approach is to model the input forces as a zero-mean white Gaussian process and make use of Bayesian techniques for state estimation (Gillijns and De Moor 2007; Lourens, Papadimitriou, et al. 2012). As is typical when implementing these methods on large scale structures, numerical instabilities arise when the number of sensors exceeds the order of the model. An augmented Kalman filter (AKF) was applied for unknown force identification in structural systems by Lourens, Reynders, et al. (2012), however the method also tends to have numerical instabilities due to unobservability issues of the augmented system matrix. Later, Maes et al. (2015) derived the conditions for the invertibility of linear system models that apply to any instantaneous input estimation or joint input-state estimation algorithm. It was demonstrated that the successive structure of the dual Kalman filter resolves the numerical issues attributed to unobservability and rank deficiency of the augmented formulation of the problem (Azam, Chatzi, and Papadimitriou 2015).

The dual Kalman filter can be used to estimate the unknown input $\mathbf{p}_k$ and state $\mathbf{x}_k$ of the linear, stochastic state space system given in Eq. (B1) using the noisy acceleration measurements $\mathbf{y}_k$.

$$\begin{aligned} \mathbf{x}_{k+1} &= \mathbf{A}\mathbf{x}_k + \mathbf{B}\mathbf{p}_k + \mathbf{w}_k^{\mathrm{x}} \\ \mathbf{y}_k &= \mathbf{C}\mathbf{x}_k + \mathbf{D}\mathbf{p}_k + \mathbf{v}_k \\ \mathbf{p}_{k+1} &= \mathbf{p}_k + \mathbf{w}_k^{\mathrm{p}} \end{aligned} \tag{B1}$$

The process noise $\mathbf{w}_k^{\mathrm{x}}$ and input noise $\mathbf{w}_k^{\mathrm{p}}$ are assumed zero-mean, white processes with covariance matrices $\mathbf{Q}^{\mathrm{x}}$ and $\mathbf{Q}^{\mathrm{p}}$, respectively. The measurement noise $\mathbf{v}_k$ is also assumed to be a zero-mean, white process. The complete filter equations are given in Table B1. The procedure needs a-priori information on the expected value $\hat{*}$ and covariance $\mathbf{P}$ of the state and input for initialization, which are then updated at each time step with new measurements.

Table B1: General scheme for time-varying DKF algorithm (Azam, Chatzi, and Papadimitriou 2015)

- Initialization at time t_0

$$\widehat{\mathbf{p}}_0 = \mathbb{E}[\mathbf{p}_0]$$

$$\mathbf{P}_0^{\mathrm{p}} = \mathbb{E}[(\mathbf{p}_0 - \widehat{\mathbf{p}}_0)(\mathbf{p}_0 - \widehat{\mathbf{p}}_0)^{\mathrm{T}}]$$

$$\hat{\mathbf{x}}_0 = \mathbb{E}[\mathbf{x}_0]$$

$$\mathbf{P}_0^{\mathrm{x}} = \mathbb{E}[(\mathbf{x}_0 - \hat{\mathbf{x}}_0)(\mathbf{x}_0 - \hat{\mathbf{x}}_0)^{\mathrm{T}}]$$

- At time t_k, for $k = 1, \dots, N_t$:
  - Prediction stage for the input:
    1. Evolution of the input and prediction of covariance input:

$$\mathbf{p}_k^- = \mathbf{p}_{k+1}$$

$$\mathbf{P}_k^{\mathrm{p}-} = \mathbf{P}_{k-1}^{\mathrm{p}} + \mathbf{Q}^{\mathrm{p}}$$

  - Update stage for the input:
    2. Calculation of Kalman gain for input:

$$\mathbf{G}_k^{\mathrm{p}} = \mathbf{P}_k^{\mathrm{p}-}\mathbf{D}^{\mathrm{T}}(\mathbf{D}\mathbf{P}_k^{\mathrm{p}-}\mathbf{D}^{\mathrm{T}} + \mathbf{R})^{-1}$$

    3. Improve predictions of input using latest observation:

$$\widehat{\mathbf{p}}_k = \mathbf{p}_k^- + \mathbf{G}_k^{\mathrm{p}}(\mathbf{y}_k - \mathbf{C}\hat{\mathbf{x}}_{k-1} - \mathbf{D}\mathbf{p}_k^-)$$

$$\mathbf{P}_k^{\mathrm{p}} = \mathbf{P}_k^{\mathrm{p}-} - \mathbf{G}_k^{\mathrm{p}}\mathbf{D}\mathbf{P}_k^{\mathrm{p}-}$$

  - Prediction stage for the state:
    4. Evolution of state and prediction of covariance of state:

$$\mathbf{x}_k^- = \mathbf{A}\hat{\mathbf{x}}_{k-1} + \mathbf{B}\widehat{\mathbf{p}}_k$$

$$\mathbf{P}_k^{\mathrm{x}-} = \mathbf{A}\mathbf{P}_{k-1}^{\mathrm{x}}\mathbf{A}^{\mathrm{T}} + \mathbf{Q}^{\mathrm{x}}$$

  - Update stage for the state:
    5. Calculation of Kalman gain for state:

$$\mathbf{G}_k^{\mathrm{x}} = \mathbf{P}_k^{\mathrm{x}-}\mathbf{D}^{\mathrm{T}}(\mathbf{D}\mathbf{P}_k^{\mathrm{x}-}\mathbf{D}^{\mathrm{T}} + \mathbf{R})^{-1}$$

    6. Improve predictions of state using latest observation:

$$\hat{\mathbf{x}}_k = \mathbf{x}_k^- + \mathbf{G}_k^{\mathrm{x}}(\mathbf{y}_k - \mathbf{C}\mathbf{x}_k^- - \mathbf{D}\widehat{\mathbf{p}}_k)$$

$$\mathbf{P}_k^{\mathrm{x}} = \mathbf{P}_k^{\mathrm{x}-} - \mathbf{G}_k^{\mathrm{x}}\mathbf{C}\mathbf{P}_k^{\mathrm{x}-}$$